MATERIALS SCIENCE AND ENGINEERING

A Publication of the University of Miskolc

MultiScience XXXIInd MicroCad International Scientific Conference
5–6 September, 2018, Miskolc, Hungary

Volume 44, Number 1

CONTENTS

MEASUREMENTS AND STUDYING CORROSION POTENTIAL OF REINFORCED CONCRETE SAMPLES PREPARED WITH AND WITHOUT A GREEN INHIBITOR AND IMMERSED IN 3.5% NaCl SOLUTION

SHAYMAA ABBAS ABDULSADA[1]–TAMÁS I. TÖRÖK[2]

In recent years the use of inhibitors in producing high performance concrete has increased significantly as a result of chloride and sulphate attacks. The effectiveness of an organic inhibitor extracted from a cheap organic waste of orange peel (so-called "green" inhibitor) was added to the fresh concrete. Two types of superplasticizers (Mapei Dynamon SR 31 and Oxydtron) were also used to reduce the water during concrete hardening. Then the concrete samples were immersed partially in 3.5% NaCl aqueous solutions for six months and every two weeks the corrosion potentials of the samples were regularly measured against a saturated calomel electrode. Results showed that the samples with Oxydtron had better ability to resist corrosion than the samples prepared with Mapei Dynamon SR 31, and samples with green inhibitor had less negative corrosion potentials (and even less with increasing concentration of inhibitor) than that of the reference sample (0% inhibitor).

Keywords: Steel reinforcement, orange peels, corrosion properties, superplasticizer

INTRODUCTION

Corrosion of steel in reinforced concrete is an electrochemical process that causes the dissolution of iron to form a range of solid products. Corrosion products is a complex mixture of iron oxides, hydroxides and hydrated oxides that evolves according to the prevailing local environment. Depending on their level of oxidation and the availability of moisture, corrosion products have specific volumes ranging from about two to six times that of the iron consumed. As such, the main damage caused by corrosion of reinforcement in concrete is not the loss of steel cross-section, but cracking of the concrete cover due to expansive stresses exerted by the continued deposition of corrosion products near the steel-concrete interface. This leads to progressive deterioration and even spalling of the cover [1–6]. In general, there are six phases in the concrete corrosion process for nondestructive monitoring of the service life of a concrete structure, as depicted in *Figure 1* [7].

---

[1] Institute of Metallurgy, University of Miskolc
   H-3515 Miskolc-Egyetemváros, Hungary
   qkosha86@uni-miskolc.hu
[2] Institute of Metallurgy, University of Miskolc
   H-3515 Miskolc-Egyetemváros
   fektt@uni-miskolc.hu

However, not all corrosion products contribute to the build-up of stresses and initial cracking of the cover. Despite the apparent insolubility of the final corrosion products, the process of corrosion involves soluble species that can dissolve in the concrete pore solution and subsequently migrate or diffuse through the cement paste matrix away from the corroding steel. In the presence of chloride ions, the dissolution of iron is increased by formation of intermediary chlorocomplexes, i.e. 'green-rusts'. These soluble complexes migrate away from the anodic sites, and subsequently break down in oxygen-rich areas, releasing the chlorides to transport more ferrous ions from the corroding steel. The mobility of these soluble species and subsequent precipitation in oxygen-rich areas results in the corrosion products being distributed within the porous cement paste [8–10].
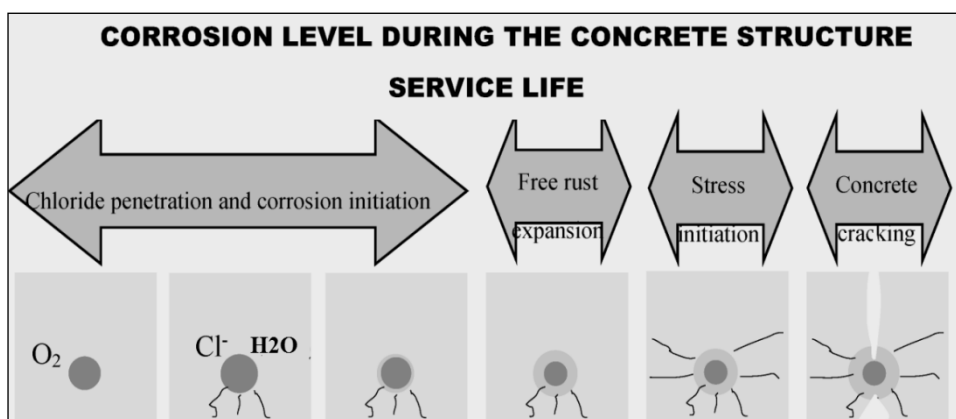
Figure 1
Schematic illustration of the various steps of the concrete deterioration due to the corrosion of the reinforcement [7]

The main purpose of this paper is to present an experimental study by utilizing non-destructive measurements, i.e. potential testing (ref. to a SCE) to monitor and evaluate corrosion processes in the steel rebar used in reinforced concrete with green inhibitor and two types of superplasticizers.

1. MATERIALS AND METHODS

1.1. Materials and Samples Preparation

Portland slag cement CEM II/A-S 42.5 R was used in this study conforming to the EN 197-1 [11] and it received from CRH Magyarország Kft. company in Miskolc. Aggregates (fine and coarse) were used according standard EN 12620 [12] and it was also received from the CRH company. Orange peels as a green inhibitor and two types of superplasticizers (Mapei Dynamon SR 31 and Oxydtron) were used. Steel rebar samples were obtained from the ÓAM steel producing company operating in

Ózd city, Hungary with diameter of 8 mm. For both making and curing the specimens tap water was used.

Concrete mixes were designed in accordance with the European mix design method (XD3 class) to have compressive strength C35/45 at age of 28 days. Two times three samples were prepared (with the two different plasticizers) and the two sets of three and three samples contained in 0%, 1%, 3% the green inhibitor as well. The reinforced concrete cubes so prepared for potential testing had dimensions of 150×150 mm and each concrete cube was reinforced with three (8 mm diameter) straight steel wires. The three bars in each reinforced concrete sample were arranged at the corners of an equilateral triangle with 8 cm sides as shown in *Figure 2*.

The molds were thoroughly cleaned and oiled before casting to avoid adhesion with the concrete surface. Mixing of materials was done manually after that water added to the mix with continued mixing, then the mix was put in the molds.

Figure 2
*Preparation and casting specimens*

The specimens were taken out from the molds after 24 hours hardening, then were immersed partially in 3.5% NaCl solution.

1.2. Corrosion Potential Measurements

An outer area of about 825 cm² of the concrete samples immersed in 3.5% NaCl solution was exposed to direct chloride attack and their upper parts (~10 cm) were above the salt water level as shown in *Figure 3*.

The corrosion potential is basically an indirect indication of the corroded state of the concrete embedded steel rebars and being verified by many previous chloride-activated accelerated corrosion tests [13]. In our case the electrochemical cell used

for corrosion potential measurements was composed of the working electrodes (i.e. the protruding reinforcement steel bars shown in *Figure 3*), and a saturated calomel electrode (SCE) used as reference electrode.
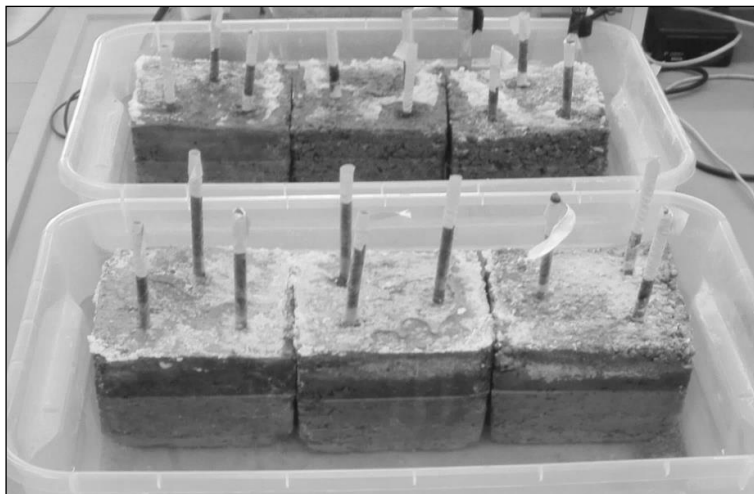
Figure 3
Specimens prepared for corrosion potential testing being immersed partially in 3.5% NaCl solution

The corrosion potential of the reinforced concrete specimens was measured every two weeks according to BS EN 1504 [14] with a (Metrix MTX 3250 Bench Digital Multimeter) by recording the potential of each wire embedded in the concrete sample shown in *Figure 4*. The average of three readings was recorded in mV units reference to the SCE electrode. For comperison the concrete corrosion potential thresholds for protection of embedded steel reinforcement are given in *Table 1*.

Figure 4
*Corrosion potential testing setup with the salt water immersed specimens*

Probability of corrosion related to the measured corrosion potentials against a Saturated Calomel Electrode (SCE) [13]

Corrosion potential (mV)	Interpretation
> −124	Low probability (10%) of corrosion
−124 to −274	Corrosion activity (50%)
< −274	High probability (90%) of corrosion

2. RESULTS AND DISCUSSION

2.1. Corrosion potentials of samples with Mapei Dynamon SR 31 superplasticizer

According to the results given in *Table 2* and *Figure 5*, the reference sample (A1) showed a greater difference in the measured corrosion potentials compared to the other samples (B1, C1). The samples containing green inhibitors had even less negative potentials compared to the reference sample (0% inhibitor).
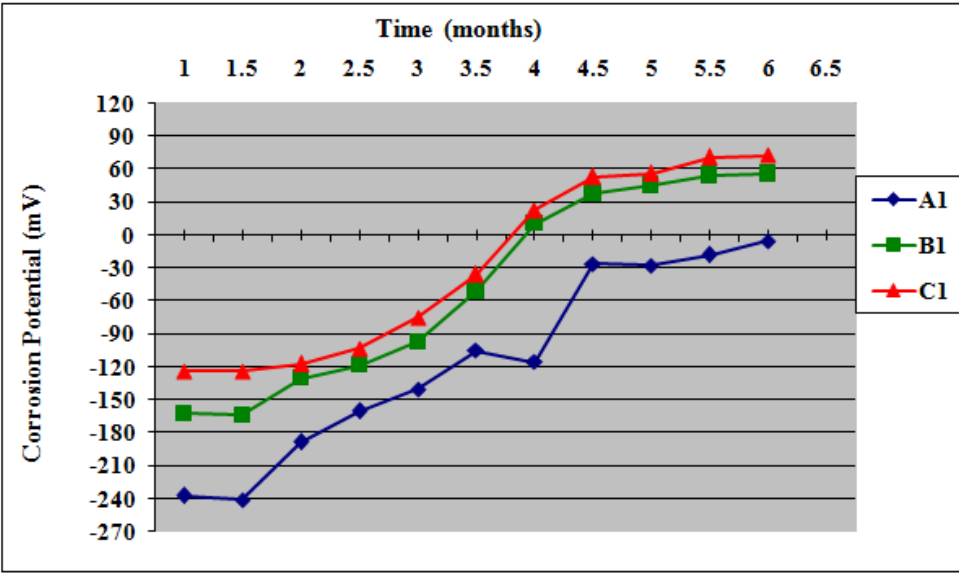
Figure 5

Corrosion potentials versus time of the steel reinforced concrete samples with Mapei Dynamon SR 31 superplasticizer

Corrosion potentials of the embedded steel specimens (with Mapei Dynamon SR 31 superplasticizer) measured in regular time intervals

| Symbol of Sample	Corrosion Potential (mV) of Samples after Different Immersion times (months) in 3.5%NaCl Solution					
	1	2	3	4	5	6
A1	−237.6	−188.4	−140	−115.5	−28	−5.4
B1	−162.5	−130.4	−97.2	10.3	45.6	55.7
C1	−123.8	−117.3	−75.2	22.7	55.8	72.5

2.2. Corrosion potentials of samples with Oxydtron superplasticizer

It's clear from *Table 3*, the reference sample (A2) have corrosion potential more negative than samples with green inhibitors (B2, C2).

Corrosion potentials of the embedded steel specimens (with Oxydtron superplasticizer) measured in regular time intervals

Symbol of Sample	Corrosion Potential (mV) of Samples after Different Immersion times (months) in 3.5%NaCl Solution					
	1	2	3	4	5	6
A2	−170.6	−125.7	−100.3	−25.8	10.9	12.7
B2	−122.3	−100.8	−34.8	15.4	49.7	55.7
C2	−120.8	−50.3	−12.7	32.7	85.4	89.6
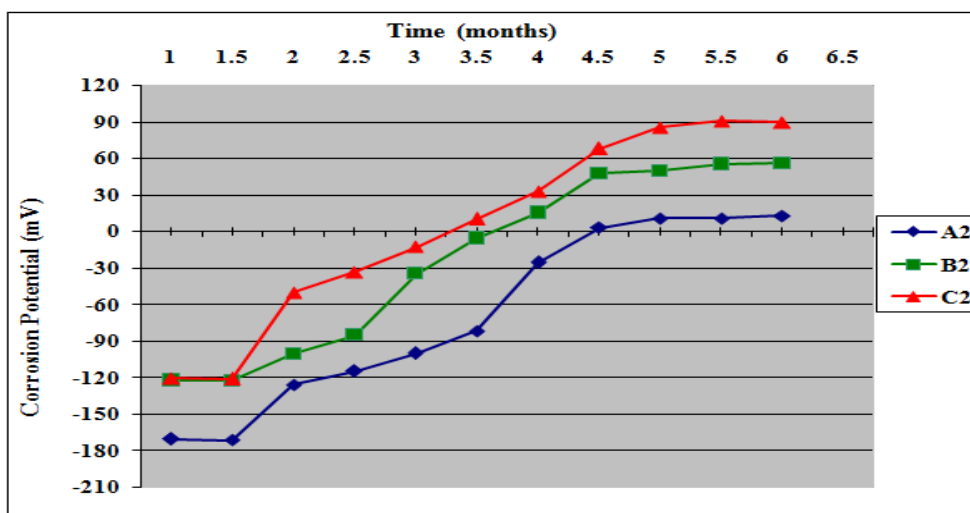
Figure 6
Corrosion potentials versus time of the steel reinforced concrete samples with Oxydtron superplasticize

The potential results obtained for samples A1 and A2 were more negative in comparison to the samples with green inhibitor, but the sample with Oxydtron (A2) was better than sample with Mapei Dynamon SR 31 superplasticizer after 6 months immersion in 3.5% NaCl.

For all samples the measured potentials became consistently less negative with increasing age of the tested specimens. This observation may be attributed to the well-known passivation phenomena of the steel rebar specimens slowly developing also in such an environment (i.e. in the concrete pore solution containing dissolved oxygen as well) through the formation of different and loosely adherent non-soluble surface corrosion products (like γ-FeOOH, γ-Fe$_2$O$_3$ and other rust components) in conjunction with the reduction of the concrete permeability due to both the loss of internal (pore) moisture and the continuing chemical formation of solid hydration products in the course of the protracted concrete hardening process.

Although it falls a bit outside of the scope of the present discussion, but it is at least worth mentioning here, that long-term analysis and final examination of the broken concrete blocks after the completion of the still running potential testing, may provide further insight into the mechanisms associated with the above presented results of the given sets of corrosion potential measurements.

According to Naish et al. [15], such corrosion potentials are very sensitive to the actual ambient environment, especially the oxygen concentration at the interface between the reinforcing steel and the concrete. In fact, the most challenging aspect of on-site potential measurements on real outside concrete structures, by means of the same testing techniques as applied by us in the laboratory on small concrete specimens with inserted short steel rods, is the fact that the corrosion potential (and corrosion current as well) are weather-dependent and, therefore, its actual value will depend on the particular climatic conditions around the reinforced concrete structure [16]. For instance, the potential will shift to more negative values when the concrete cover becomes saturated by rainfall. Studies of bridge decks in Europe, where waterproofing membranes are used, or where de-icing salts are applied less frequently, have resulted in a different set of interpretive guidelines [17]. Usually, a decrease in oxygen (O$_2$) can drive the corrosion potential significantly towards more negative values. Such observations collected from longer-time monitoring of the corrosion potential (and current) schemes with time on real concrete structures can also help us interpret our laboratory observations correctly. Anyhow, in this respect it is promising that our laboratory samples having 1 & 3% green inhibitor (i.e. samples B2 & C2) showed even better behavior than the samples B1 & C1, most probably due to the synergistic effect of the Oxydtron superplasticizer together with the tested green inhibitor.

CONCLUSION

During our laboratory experiments the tested concrete samples with orange peel extract have shown more promising positive effect with Oxydtron superplasticizer than with the SR 31 superplasticizer especially in sample C2, because the chemical composition of the Oxydtron (by help forming stronger bounds and lower porosity) leads to keep the water ratio in the fresh concrete mix for longer time before hardening, therefore, the concrete will have enough time for the 'proper' evolution of the hydration bonding reactions (with the required products like C3S, C2S, C3A, C4AF) resulting also in a more advantageous capillary porosity. The addition of a green inhibitor, this inhibitor works as a retarder, meaning that it retards the action of C3S or C3A and this action causes improved properties of the concrete samples due to greater fines content and a wide range of particle distribution which are important parameters to give a more closed/compact structure and decreased capillary porosity.

And, eventually, all these factors will lead to low diffusion of chloride inside the samples and lower risk of corrosion.

REMARK

The content of this paper has been partly presented at the MultiScience XXXIInd MicroCad International Scientific Conference, 5–6 September, 2018, Miskolc, Hungary.

REFERENCES

[1]   Abdulsada, Shaymaa Abbas, Török, Tamás I., Fazakas, Éva (2018). Preliminary Corrosion Testing of Steel Rebar Samples in 3.5% NaCl Solution with and without a Green Inhibitor. *Építőanyag – Journal of Silicate Based and Composite Materials*, Vol. 70, No. 2.

[2]   Talbot, D., Talbot, J. (1998). *Corrosion Science and Technology*. London: CRC Press.

[3]   Bentur, A., Diamond, S., Berke, N. S. (1997). *Steel Corrosion in Concrete, Fundamentals and Civil Engineering Practice*. Taylor & Francis.

[4]   Bertolini, L., Elsener, B., Pedeferri, P., Polder, R. (2004). *Corrosion of Steel in Concrete*. Wiley.

[5]   ACI Committee 222 (2005). *Protection of metals in concrete against corrosion*, ACI 222R-01, ACI Manual of Concrete Practice.

[6]   Broomfield, J. P. (2007). *Corrosion of steel in concrete, understanding, investigation and repair*. Second ed., London: Taylor & Francis, London.

[7]   Naasson, P., Alcantara, Jr., Silva, M. F., Guimar, T. M. & Pereira, D. M. (2016). Corrosion Assessment of Steel Bars Used in Reinforced Concrete Structures by Means of Eddy Current Testing. *Sensors,* 16, 15, pp. 1–18.

[8]   Sagoe-Crentsil, K. K., Glasser, F. P. (1989). Steel in concrete: part I. A review of the electrochemical and thermodynamic aspects. *Mag. Concr. Res.*, 41, pp. 205–212.

[9]   Glasser, F. P., Sagoe-Crentsil, K. K. (1989). Steel in concrete: part II. Electron microscopy analysis. *Mag. Concr. Res.*, 41, pp. 213–220.

[10]   Sagoe-Crentsil, K. K., Glasser, F. P. (1993). Green corrosion products, iron solubility and the role of chloride in the corrosion of steel at high pH. *Cem. Concr. Res.*, 23, pp. 785–791.

[11]   EN 197-1, Cement-Part 1: *Composition, specifications and conformity criteria for common cements*, European Standard was Approved by CEN National Members on 21 May 2000.

[12]   EN 12620, *Aggregates for Concrete*, European Standard was Approved by CEN National Members on September 2002.

[13]   Ribeiro, D. V., Labrincha, J. A., Morelli, M. R. (2012). Effect of red mud addition on the corrosion parameters of reinforced concrete evaluated by electrochemical methods. *IBRACON Structures and Materials Journal,* Vol. 5, No. 4, pp. 451–458.

[14]   BS EN 1504, Basics of Concrete Repair and Structural Strengthening, Structural Concrete Alliance, Concrete Repair Association, on this web: http://www.sca.org.uk/pdf_word/Penrith%202015/Basics%20of%20Concrete %20Repair%20and%20Structural%20Strengthening.pdf

[15]   Naish, C., Harker, A. & Carney, R. F. A. (1990). Concrete inspection: Interpretation of potential and resistivity measurements. *Proceedings for Corrosion of Reinforcement in Concrete*. Elsevier Applied Science, pp. 314–332.

[16]   Andrade, C. & Alonso, C. (2001). On-Site Measurements of Corrosion Rate of Reinforcements. *Construction and Building Materials*, Vol. 15, No. 23, pp. 141–145.

[17]   Jefremczuk, Sandra (2004). *Chloride Ingress and Transport in Cracked Concrete*. MSc thesis, Mc Gill University, Canada, p. 97.

TENSILE ANALYSIS OF 3D PRINTER FILAMENTS

DÁVID HALÁPI[1]–SÁNDOR ENDRE KOVÁCS[2]–HENRIETTA HUDÁK[3]–
ZSOLT BODNÁR[4]–ÁRPÁD BENCE PALOTÁS[5]–LÁSZLÓ VARGA[6]

The objective of this research is to characterize the materials which has been produced by a 3D printing technology, namely Fused Deposition Modelling (FDM). All of the chosen materials are reinforced by another material (e.g. glass fiber or metal powder), and the reinforced material is present in different weight fractions. Like the 3D printing technologies in general, FDM builds up the speciments layer by layer following a predefined orientation, and the main assumption is that the materials are behaving similarly to laminates formed by orthotropic layers. Great emphasis must be put on the selection of the appropriate quality filaments, therefore fist the material properties of the fibers were examined. The first testing method was tensile strength analysis, which has been followed by scanning electron microscopy (SEM), to observe francture surfaces. After SEM analysis, it became clear that the morphology of the fibers are material dependent. This answer was given by the microstructure of the filaments. The difference as well as the diverse types of the fibers explains the variability in material properties among the examined test materials.

Keywords: PLA, mechanical properties, 3D printing, additive manufacturing, tensile tests

INTRODUCTION

A 3D prototype manufacturing became quite widespread nowadays, a lots of manufacturer offers various printers with different solutions, at an available price. One can 3D print virtually anything and everything. [1]
Prototype production can be categorized into three groups:
- Formative manufacturing (e.g., casting, plastic forming);
- Subtractive manufacturing (e.g., forging, turning, routing etc.);
- Additive manufacturing (3D printing etc.).

---

[1] Department of Foundry Institute, University of Miskolc
     H-3515 Miskolc-Egyetemváros, Hungary
     ontdavid@uni-miskolc.hu
[2] Department of Foundry Institute, University of Miskolc
   H-3515 Miskolc-Egyetemváros, Hungary
[3] Institute of Foundry, University of Miskolc, H-3515 Miskolc-Egyetemváros, Hungary,
     ontheni@uni-miskolc.hu
[4] Philament Ltd. Miskolc
[5] Department of Combustion Technology and Thermal Energy, University of Miskolc
     H-3515 Miskolc-Egyetemváros, Hungary
     arpad.palotas@uni-miskolc.hu
[6] Department of Foundry Institute, University of Miskolc
     H-3515 Miskolc-Egyetemváros, Hungary
     ontvlaci@uni-miskolc.hu

In this paper we will discuss additive manufacturing in detail. *Figure 1* shows the available 3D printing technologies. Fused Filament Fabrication (FFF) technology was selected for this set of experiments. As a comparison, SLA subjects made by SLA technology was also analyzed. Our goal was to select the process that produces the best tensile strength results.
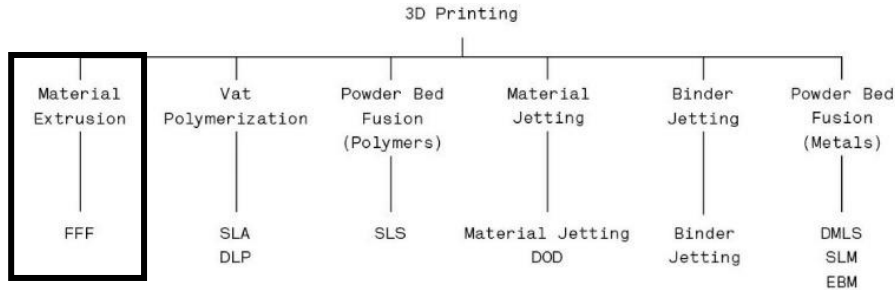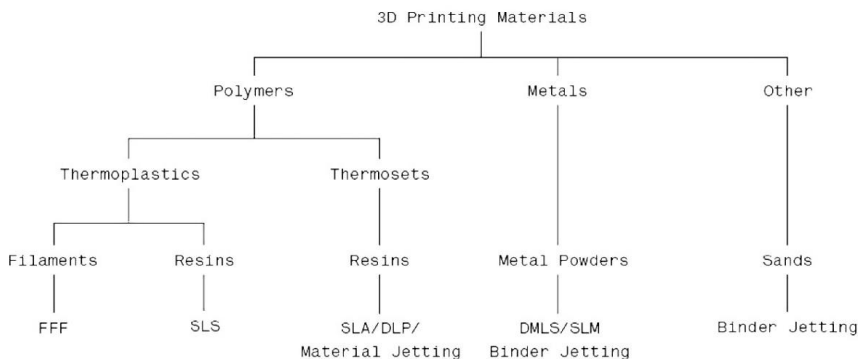

Figure 1
Additive 3D technologies [2]

Each 3D printing process uses different materials (shown in *Figure 2*). It is clear, that the chosen technology, the FFF process, is based on polymer based materials. During the analysis mechanical properties were tested of these two kinds of polymer based materials, the thermoplastics and the thermosets. [3]

Our current study focuses on thermoplastic printing technology, using PLA as a base material, as for future plans, we are planning to compare the differences between the two groups.

Several literature and scientific articles are starting to deal with metal-printing 3D printer machines, which are building up the structure from metal powder. This area of 3D printing is extremely popular nowadays, however extremely expensive as well. The advantage of this process, that the product even usable instantly after printing.

Figure 2
Material classification of 3D printing [2]

Figures 3–4 illustrates two comparisons, one, characterising the 3D printed object by function and the other being the visual appearance/surface quality. It is essential to choose the printer technology according to what is more important. As stated above, each process has its own materials, and thus each has its own strengths and weaknesses. One always have to keep in mind what to achieve by printing something.

As it can be seen in *Figure 3*, which breaks down the classification according to applicability and special properties, the two main factors are the dimensional accuracy and the strength. The dimensional accuracy is a very important factor in prototype and component production. A designed component is only economical, if the accuracy has a narrow tolerance field. In 3D printing, the accuracy and layer thickness are in relation to each other.
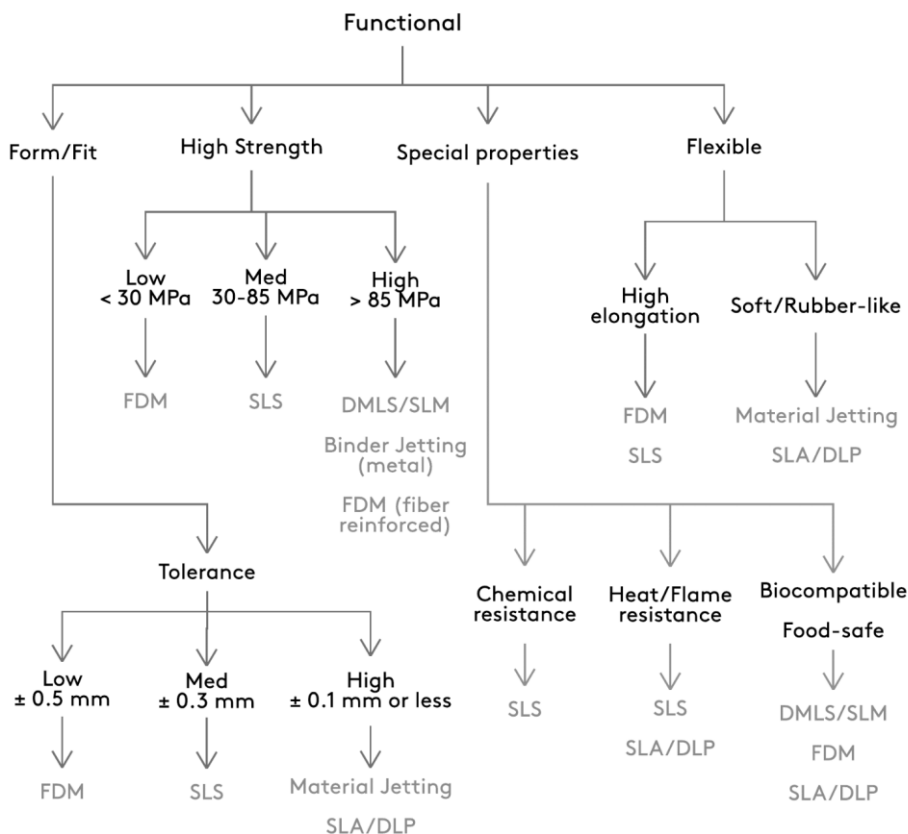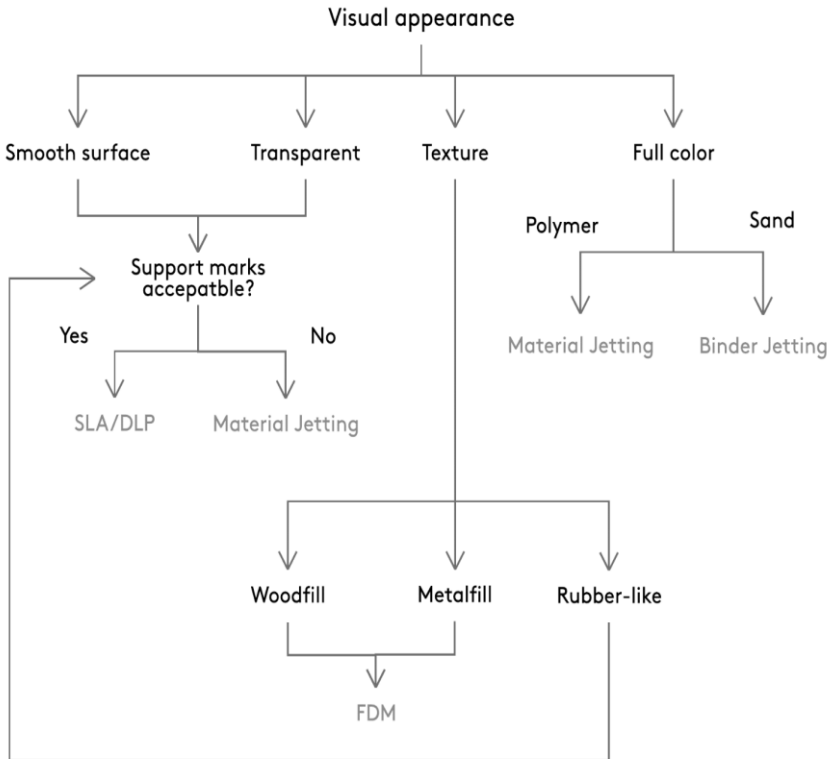

Figure 3
Classification according to applicability and special properties [2]

Our primary goal is compare the available strength data of the newer types of filaments' properties. As *Figure 3* states, some of the 3D printed objects made of these filaments exhibit up to 30 MPa tensile stress.

When testing filaments enhanced by additive materials, the tensile stress properties of the specimens can exhibit as high as 50 MPa. As for visual appearance, the FDM filaments have strong potentials in the textured raw materials section.

Figure 4 shows the groups of the surface types. Generally speaking, the main criterion for a manufactured component is the surface quality. However, there are different needs also, for example materials with textured surface (wood, metal) effect. Other printing method can be the usage of tinted raw material.

Figure 4
Variety of visual appearance [2]

The PLA polymer threads basically have low tensile stress properties; however, they are available at a very attractive price. *Figure 5* shows the comparison between the fiber materials for semi-crystalline and amorphous structures. The other categorization possibility is based on the strength properties. There are general materials, engineering materials, with advanced strength properties, and high performance materials.

Figure 5 shows how different can be a 3D printed material depending its field of use. While most of the printed goods are in the commodity field, which means that it is the most common and economical, engineering and high-end usage requires

more complex solutions. Complex solutions require higher printing temperature and of course more money to make, but this way the performance of the printed part greatly increases.

PEEK and PEI are top notch materials and offer great performance over extreme temperatures and various conditions.
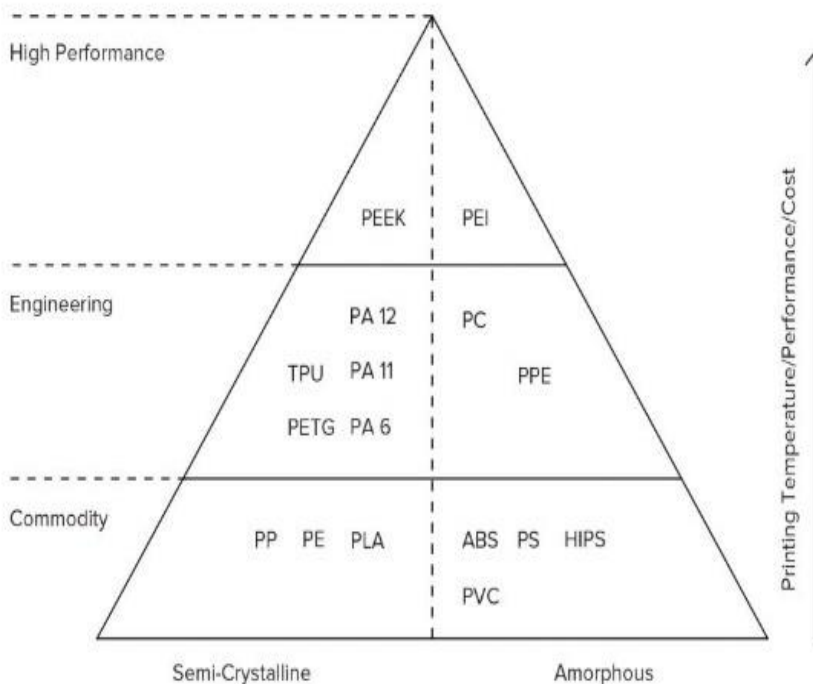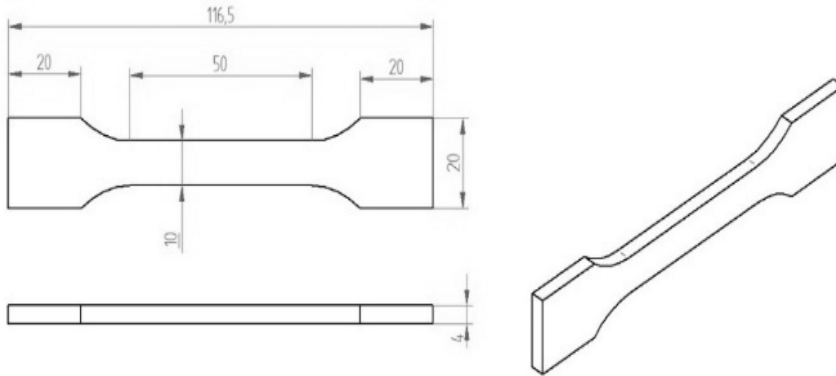

Figure 5
Categorization of 3D Materials by Field of Application [2]

1. MATERIALS AND METHODS

For analysis 6 different FDM filaments were tested. Our goal was to compare the tensile strength properties of the PLA poly(lactic acid) based materials some of them with different additive materials. Two different methods were used: first, the tensile stress test specimens were compared, then the stress properties of each filament materials were analyzed. During the tests each thread's outer diameter was 1,75 mm. Printing was executed by a Cetus MKII extended 3D printer. As for the first wave of test specimens the printer's basic settings were used during the printing process, with 100% filling. The printed tensile strength test specimen were made according to the ISO 3167 1994 standard's parameters, with a thickness of 4 mm. Tensile tests were performed with an Instron 5566 type tensile machine. The measurements were performed at 50 mm/min speed at room temperature. These details are shown in *Figure 6*. The threads contained the following additive materials: [4]
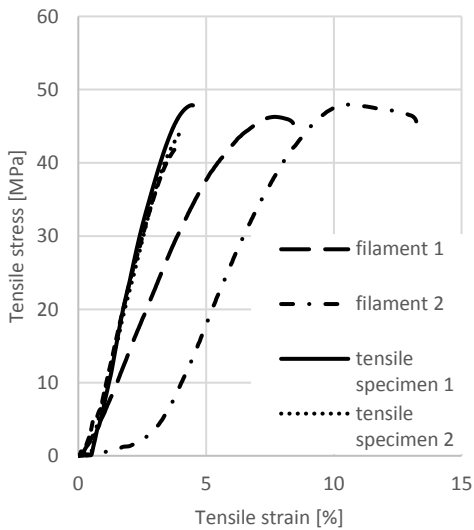
- White – chalk powder
- Black – "technical"
- Blue – 5% glass fiber
- Red – basic PLA
- Glass – 15% glass fiber
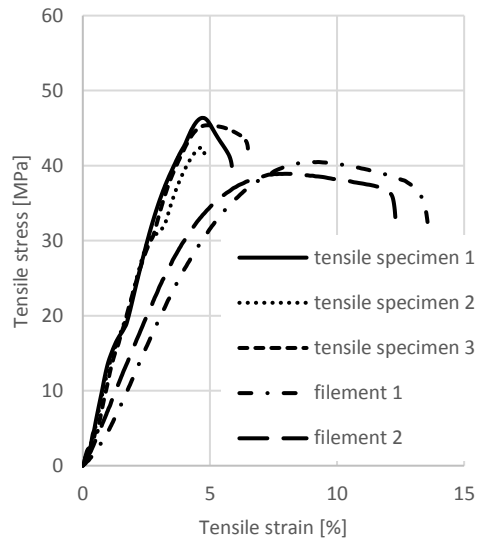- Metal 10% – 10% metal powder

Figure 6
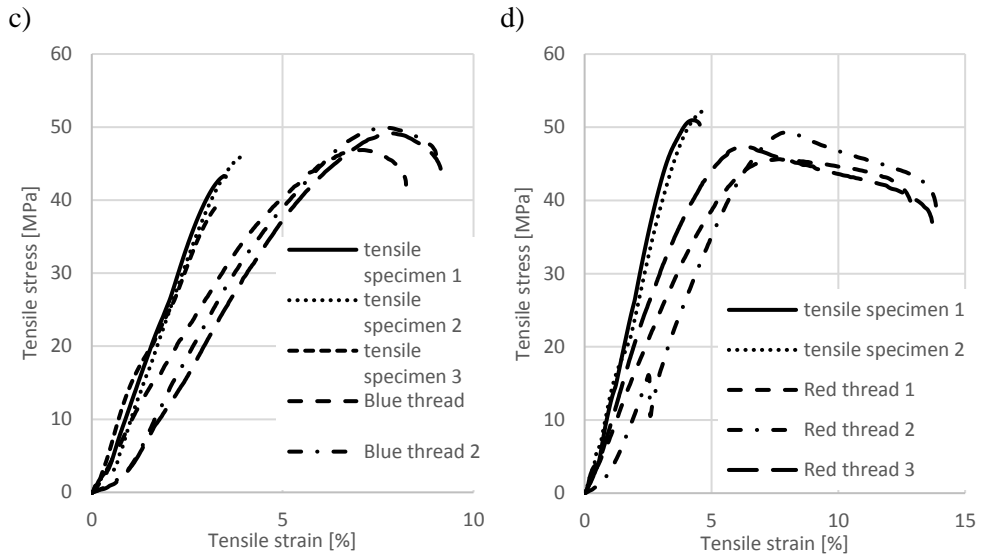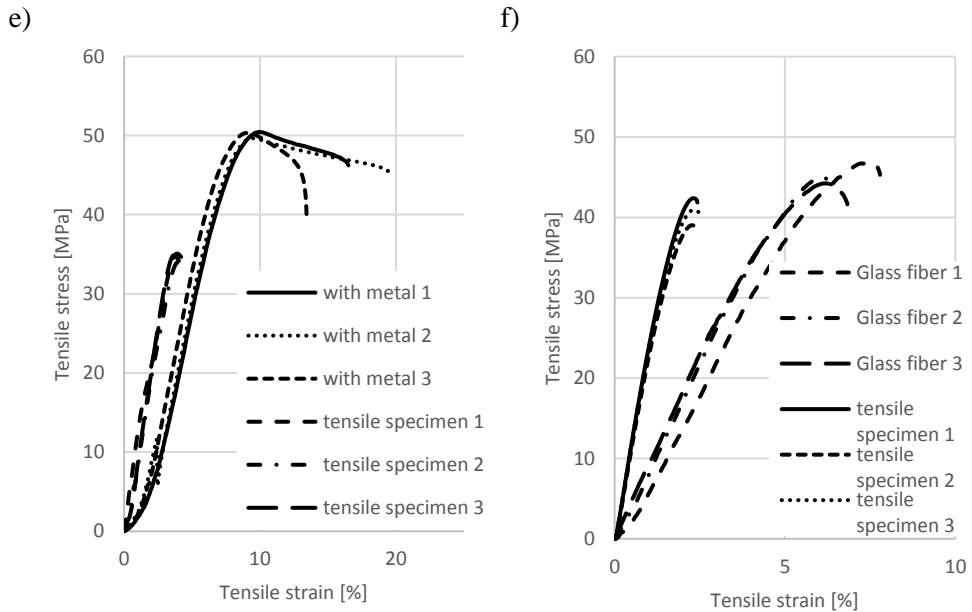*ISO 3167 1994 specimen* [7]

2. RESULTS AND DISCUSSION

a)

b)

Figure 7
Tensile test results of – a) white, b) black filament

c)

d)

Figure 8
*Tensile test results of – c) blue, d) red filament.*

e)

f)

Figure 9
Tensile test results of – e) metal 10%, f) glass fiber filament

Results of the experiments are summarized in *Figures 7–8–9.* One can clearly note, that the printing procedure weakens the material, i.e., the tensile strength of a printed
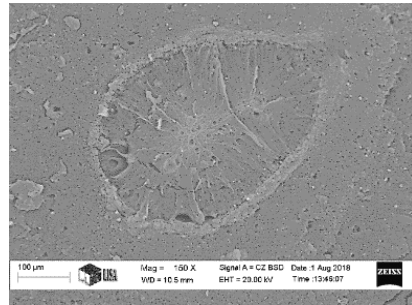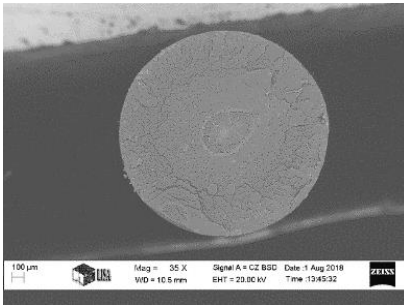
specimen is lower than that of the original filament thread when there is an additive in the material.

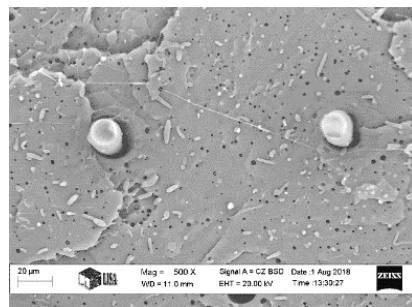Scanning electron micrographs (SEM images) of the various filament threads are shown in *Figures 10–15.*
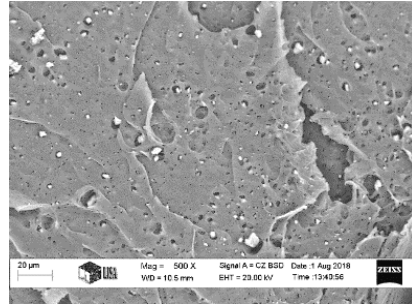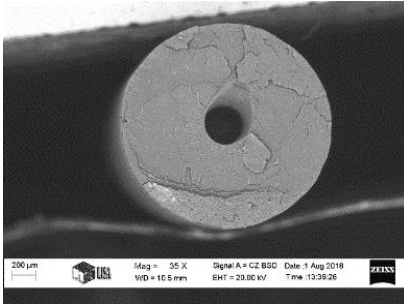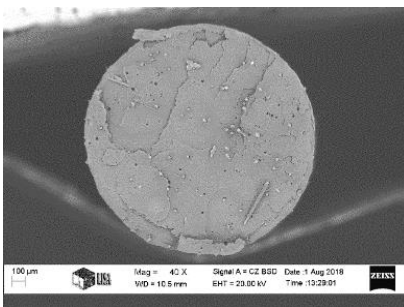

Figure 10
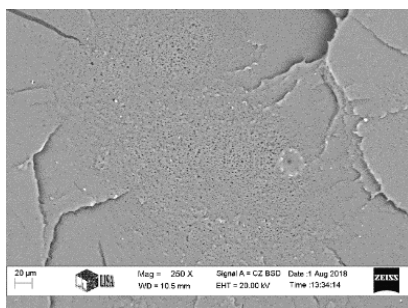*Cross section of the PLA (White) filament by SEM nominal magnification 35×; 500×*
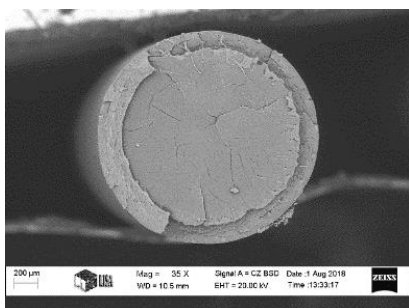

Figure 11
Cross section of the PLA (Black) filament by SEM nominal magnification 35×; 150×

Figure 12
Cross section of the PLA (Blue) filament by SEM nominal magnification 40×; 500×

Figure 13
Cross section of the PLA (Red) filament by SEM nominal magnification 35×; 250×
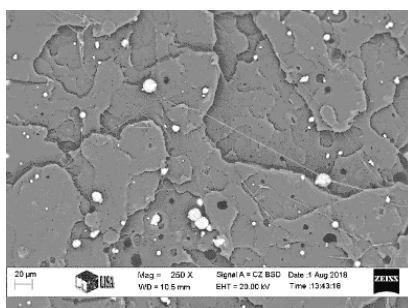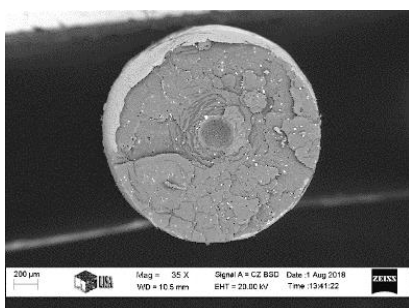
Figure 14
*Cross section of the PLA+10% metal powder filament by SEM nominal magnification
35×; 250×*
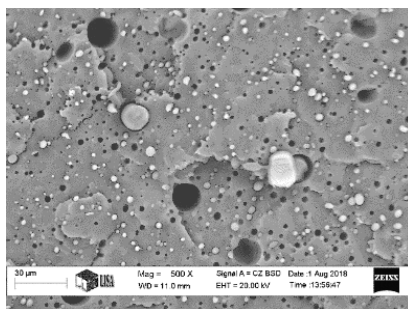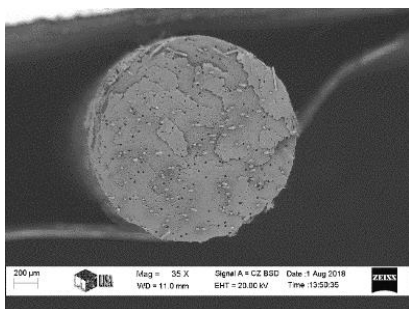
Figure 15
*Cross section of the PLA+glass fiber filament by SEM nominal magnification
35×; 500×*

CONCLUSION

Measurement data suggests that the printing process deteriorates some of the mechanical properties, i.e., namely the tensile strength value of the printed specimen is lower than that of the original filament thread of PLA with reinforcement additive. This finding seems to be additive independent.

REMARK

The content of this paper has been partly presented at the MultiScience XXXIInd MicroCad International Scientific Conference, 5–6 September, 2018, Miskolc, Hungary.

REFERENCES

[1]   Kietzmann, J., Pitt, L. & Berthon, P. (2015). Disruptions, decisions, and destinations: Enter the age of 3-D printing and additive manufacturing. *Bus. Horiz.*, Vol. 58, No. 2, pp. 209–215.

[2]   Redwood, B., Schöffer, F. & Garret, B. (2017). *The 3D Printing Handbook*. 3D Hubs, p. 304.

[3]   Berman, B. (2012). 3-D printing: The new industrial revolution. *Bus. Horiz.*, Vol. 55, No. 2, pp. 155–162.

[4]   Bodnár, Zsolt. *Philament Technical materials*. [Online]. Available: www.philament.eu. [Accessed: 14-Aug-2018].

[5]   Tóth Dénes (2015). *Prototípusgyártás FDM eljárással*. (Thesis) University of Miskolc.

[6]   Ferreira, R. T. L., Amatte, I. C., Dutra, T. A. & Bürger, D. (2017). Experimental characterization and micrography of 3D printed PLA and PLA reinforced with short carbon fibers. *Compos. Part B Eng.*, Vol. 124, pp. 88–100.

[7]   INTERNATIONAL STANDARD ISO. Vol. 2002.

NEUTRAL, ACID AND ALKALINE LEACHING OF TYPICAL THERMO-MECHANICALLY TREATED ALUMINIUM MELTING DROSS RESIDUES

BALÁZS HEGEDÜS[1]–TAMÁS KÉKESI[2]

A large amount of currently useless – basically oxide – residue is produced by the treatment of dross obtained from the melting of alloyed aluminium scrap. Its negligible residual metallic content does not make it feasible for any further metallurgical processing. On the other hand, it may contain chloride salts, whose removal may not only serve the purpose of recycling but it is required to make this residue suitable for alternative applications, such as construction and road paving materials, or slag forming additive in the steel industry. A hydrometallurgical treatment with pure water can be efficient in this respect and applying acidic or alkaline media can even reduce the residual metallic content. The composition of the raw residue was examined by instrumental techniques and experiments were carried out to determine the efficiencies of the treatments with water, sulphuric acid and sodium hydroxide. Leaching with water could remove the main salt components of NaCl and KCl in a short time. However, some NH_3 is evolved from the reaction of AlN formed during the preliminary thermo-mechanical treatment. The application of sulphuric acid can be efficient not only in removing the residual metal content but also in suppressing the evolution of NH_3. Although the sodium-hydroxide reagent is capable of aggressively dissolve aluminium not only in the metallic but also in the oxide states, but it also enhances the evolution of NH_3. According to the phase composition and structure of the treated materials, water leaching – perhaps combined with an extra step of sulphuric acid leaching – can be satisfactory for assuring the state of the residual dross to be accepted in different applications.

Keywords*: Aluminium dross, salt cake, salt removal, dross utilisation*

INTRODUCTION

For economic and environmental reasons, the use of secondary raw materials in aluminium production has been continually increasing. The recycling of obsolete products made of aluminium and aluminium based alloys by melting in reverberatory furnaces results in an increased generation of dross [1], [2]. This inevitable by-product consists of chains formed by the solid oxide particles. As there is no congruent interface, it may entrap a large amount of liquid metal mechanically [3], [4]. Thus it

---
[1]   Institute of Energy and Quality Management, University of Miskolc
     H-3515 Miskolc-Egyetemváros, Hungary
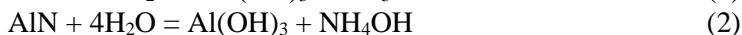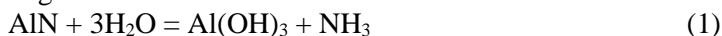   hegedus.balazs@uni-miskolc.hu
[2]   Institute of Energy and Quality Management, University of Miskolc
     H-3515 Miskolc-Egyetemváros, Hungary
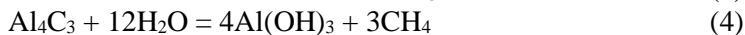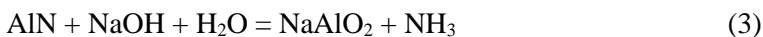   kekesi@uni-miskolc.hu

may even enhance the heterogeneous oxidation of the aluminium melt. The recovery of the high metallic content can be implemented at the production site by a thermo-mechanical treatment of the hot dross applying heat to melt the entrapped metal and mechanical action combined with salt addition to break the oxide layers insulating the molten droplets. This is usually carried out in an oxygen-gas fired rotary – "converter" – furnace. The relatively large amount of the added – usually NaCl-KCl based – salt [5] serves to help separate the oxide coatings and to prevent excessive re-oxidation of the molten metal phase. After tapping the recovered molten metal, the residual solid waste material ("residual dross") is discharged, which may contain just a few per cents of the metallic phase [3]. Thus it may not be economically processed by the usual metallurgical processes [6]. In its usual state, it does not constitute any commercially significant value, rather it may mean a burden both from the financial and environmental aspects. Nevertheless, other industries (such as construction and road paving materials production, cement clinkering, chemical industry, steel making with synthetic slags, mineral wool production, agriculture and glass manufacturing) may use the basically oxide containing residue if the unwanted components, mainly the relatively large amounts of salt [7], can be removed efficiently. The almost negligible portion of dispersed aluminium metal particles are covered by thick and refractory oxide layers, therefore they do not cause much trouble even for the applications in the construction materials industry, but it may even be beneficial when steel making or glass foam producing applications are proposed.

The salt content – composed of mainly chlorides – of the residual dross can be readily dissolved by pure water at ordinary temperatures, therefore it may be the fundamental and a suitable initial step in a hydrometallurgical processing scheme. The residual dross of high salt content, often referred to as salt cake, is usually black coloured. It is generally crashed and ground. It may be followed by the simple physical removal of the malleable metal grains of larger size, and the fine powder is mixed with as much water to yield a brine liquor of 20–25% saturation, which offers efficient dissolution and does not imply excessive energy requirement for the subsequent removal of water by evaporation. As a result of the exothermic reactions of dissolution, the temperature may rise to as high as 60 ºC during leaching [6]. The subsequent solid/liquid separation can be carried out in multiple steps, including a preliminary centrifuging to remove the coarser particles. The fine slurry is then settled and washed during filtration. The salt-free solid product can be suitable for the aimed alternative ways of utilization and the brine liquor can be evaporated by boiling, followed by the drying of the wet salt crystals before recycling to the thermal process in the rotary furnace. As KCl is more volatile than NaCl, the leaching of the latter by-product is also required, and some KCl may still be added to reset the original composition of the usually equimolar NaCl-KCl mixture used in aluminium melting.

The residual dross obtained from the high temperature treatment of the primary aluminium dross contains nitrides and carbides too. These compounds may also react with water during leaching:

$$AlN + 3H_2O = Al(OH)_3 + NH_3 \tag{1}$$
$$AlN + 4H_2O = Al(OH)_3 + NH_4OH \tag{2}$$

$$AlN + NaOH + H_2O = NaAlO_2 + NH_3 \tag{3}$$
$$Al_4C_3 + 12H_2O = 4Al(OH)_3 + 3CH_4 \tag{4}$$

The fine metallic particles – after the oxide coating is removed – may react with the alkaline or acidic or even the neutral aqueous medium, like:

$$Al + NaOH + H_2O = NaAlO_2 + 1.5H_2 \tag{5}$$
$$Al + 3NaOH = Na_3AlO_3 + 1.5H_2 \tag{6}$$
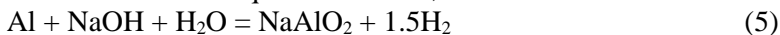
Some other dangerous gases (phosphine, hydrogen sulphide) may also be evolved. These reactions are all exothermic, and the co-existence of heat and the inflammable gases may even cause danger of fire and explosion besides poisoning. However, these effects may also be present when the residual dross is simply disposed of. There are proposed technologies [7] which are assumed to offer 99% recovery of the salt and a low (<0.2%) chloride content in the final residue, and the harmful gases evolved during the hydrometallurgical treatment are combusted. The heat from the latter step can be utilized for the evaporation of water.

1. EXPERIMENTAL PROCEDURE

As a result of the thermo-mechanical treatment of the aluminium melting dross, solid residues of different colour can be obtained. In the extreme cases they can appear light or dark, as shown in *Figure 1*. The metallic content of the lighter material is lower. In the obtained sample it was 9.9%, and it was a mere 1.1% in the fine (<250 μm) fraction obtained after grinding. Whereas these values were 13.6% and 4.5% in the dark material representing the opposite extreme quality. The metallic content in the powder fraction was finely dispersed and in particles covered by a thick oxide layer. This part of the metal content in the residual dross could be determined only by the volume of the collected hydrogen gas evolved from the reaction of aluminium with hot and concentrated NaOH solution [3], [4].
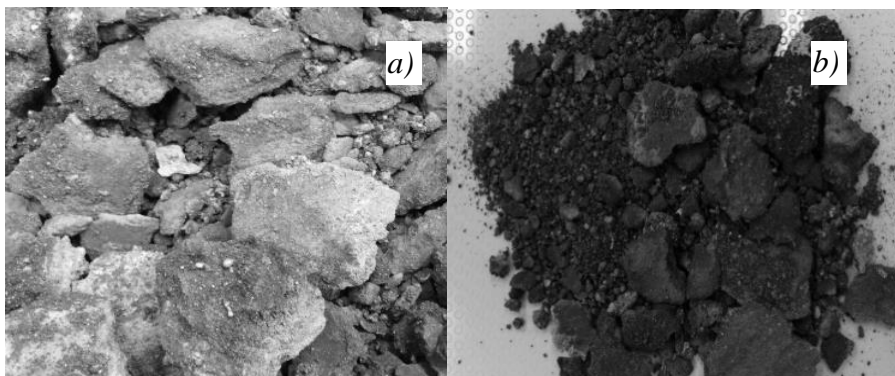
Figure 1
*The macro images of the light (a) and dark (b) coloured residues
from the thermal treatment*

1.1. The examined material

The major constituent of the two different looking types of the residual dross – serving as the principal raw materials for the experiments – were examined by scanning electron microscopic (SEM), energy dispersive X-ray microprobe (EDS) and X-ray dispersive (XRD) techniques applying the finely ground (<250 μm) fractions. The characteristic micro images and the relevant EDS spectra are shown in *Figure 2* and *3*.
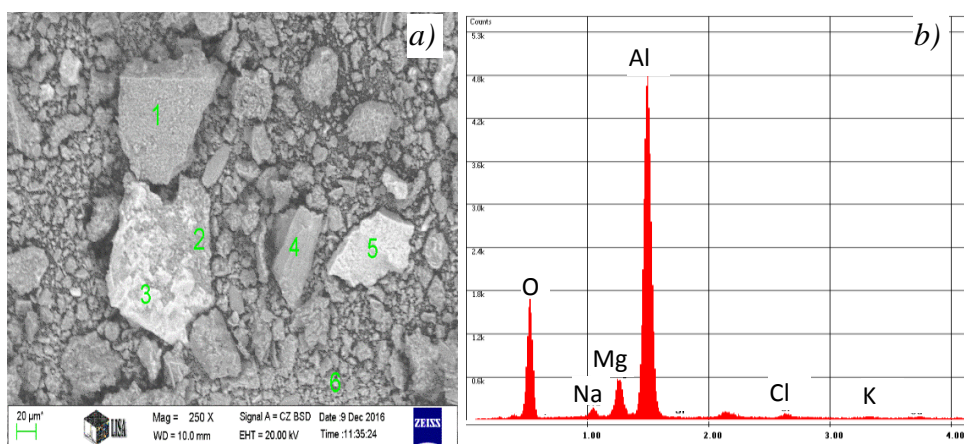
Figure 2

The SEM image (a) and the EDS spectrum (b) of the light coloured residue from the thermo-mechanical treatment
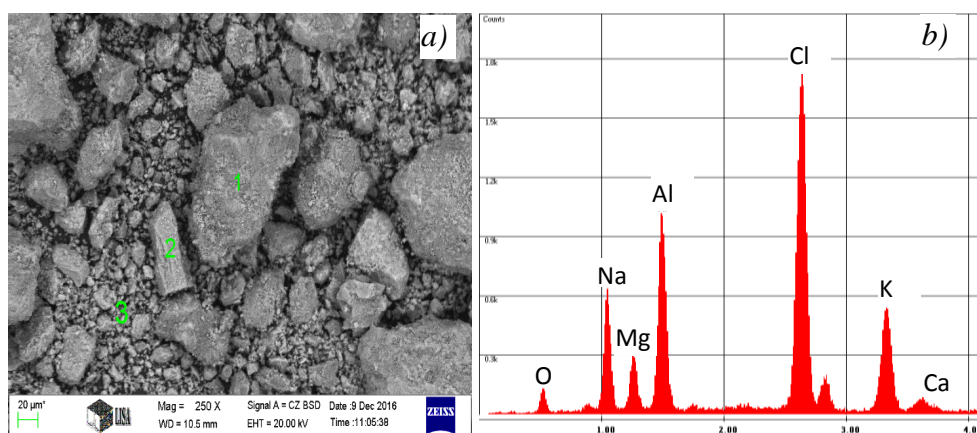
Figure 3

The SEM image (a) and the EDS spectrum (b) of the dark coloured residue from the thermo-mechanical treatment

As the electron beam can penetrate into the oxide material to a depth of ~5 µm, the core of the grains may also contribute to the spectra if the oxide coating is thinner. Besides, the X-ray emission of the larger atoms is relatively stronger, thus the Al signal is stronger than those of Na, Mg or O even at practically equal concentrations. On the other hand, the signals of Cl and Ca are relatively stronger. The EDS spectra reveal that the light coloured dross residue mainly consists of aluminium oxide, whil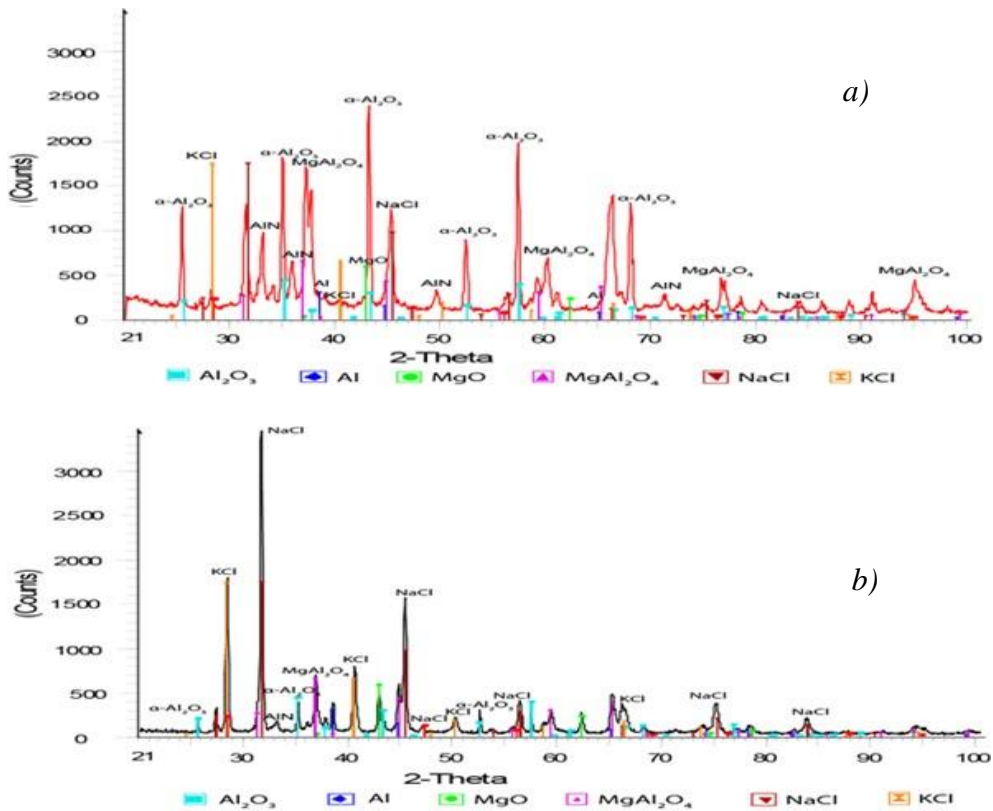e the dark coloured residue exhibits a relatively large proportion of the salt components and probably more metallic aluminium. A similar examination of the additive salt pointed out NaCl and KCl as the main components and some added CaF_2. The phase composition of the examined residual dross materials is given by the obtained XRD spectra in *Figure 4*.

Figure 4
*The XRD spectra of the light (a) and dark (b) dross residues*

The XRD spectra have proved that the simple and complex oxides ($α$-Al_2O_3 and $MgAl_2O_4$) dominate the light coloured dross residue, whereas the remaining salt content is significantly higher in the dark dross residue. The dominance of the simple oxides in the light coloured dross residue indicates the higher temperature probably

reached during the thermo-mechanical treatment, which also enhances the evaporation of especially KCl and Mg.

1.2. Leaching experiments

The finely ground dross residue samples were leached with either distilled water, 16.3 m/m% (10 V/V %) sulphuric acid or 6 mol/dm^3 NaOH solutions. The selected low H$_2$SO$_4$ concentration is preferred generally in hydrometallurgy [8], [9], [10], and the high NaOH concentration served as a reference to the strong solubilizing effect for Al$_2$O$_3$ [3], [4], [10]. Basically, the light and the dark coloured industrial dross samples were used, but further experiments were also carried out with samples obtained from laboratory thermo-mechanical treatment of different residues obtained from different primary dross samples and mixed with different amounts of salt. The 10 g samples were contacted with 100 cm^3 of the lixiviant solutions, providing safe solubility. The suitable kinetic conditions were assured by horizontal shaking to eliminate settling in polyethylene reactor vessels of 300 cm^3 volume. The kinetic leaching experiments were carried out each for 5, 15, 30, 60, 120, 180 and 240 minutes. The concentrations of the chloride and the hydrogen ions were obtained by titrimetric methods, but the concentrations of the dissolved metals were determined by atomic absorption spectrometry (AAS). The results were expressed as recoveries relative to the mass of the examined dross samples. The equipment and the steps of laboratory leaching experiments are illustrated by *Figure 5*.
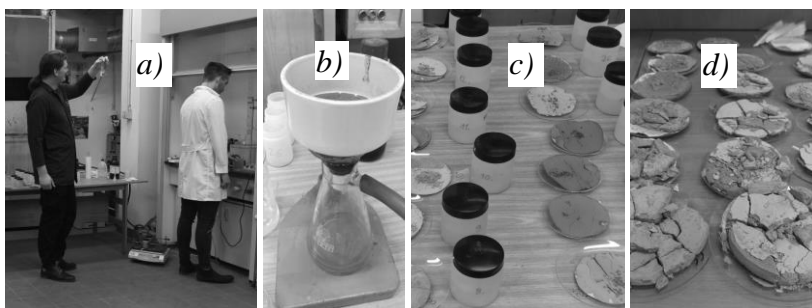
Figure 5
The fundamental leaching experiments – (a) leaching and sample preparation, (b) vacuum filtering, (c, d) solutions and solid residues from leaching

2. EXPERIMENTAL RESULTS AND DISCUSSION

Instead of common "recoveries", referring to the original contents of the components, the extraction results are expressed as "yields" referring to the mass of the sample. However, the sequential results indicate that virtually complete recoveries are usually attained.

2.1. Leaching progress

The amounts of dissolved elements yielded by various times of water leaching from the light and dark coloured residual dross samples are given in *Figure 6*.
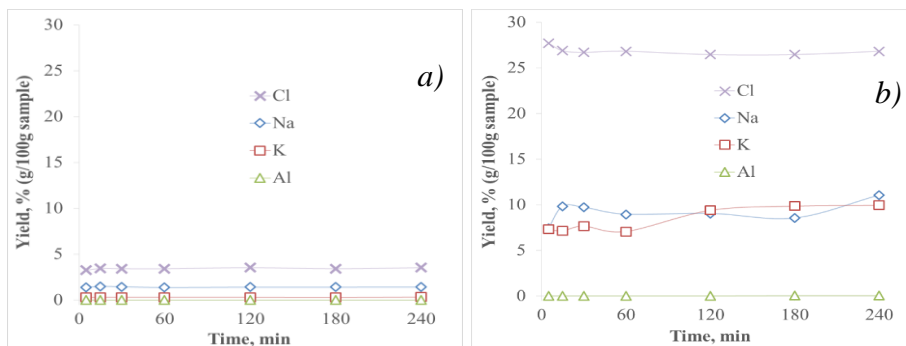
Figure 6

The yields of components by water leaching from (a) the light and (b) dark coloured dross samples obtained from the industrial hot treatment

Dissolved chlorine was analysed by an instant argentometric method to indicate the soluble salt content of the dross samples directly. As calculated from the more accurate AAS analytical results for Na and K, leaching with water could reach as much dissolved salt as ~40% relative to the sample mass of the dark residual dross. On the other hand, water leaching of the light coloured dross material yielded only slightly over 4% dissolved salt. This is a considerable difference.

It is also remarkable, how quickly the amount of the dissolved chloride salt yielded by water leaching can reach a maximum. It may imply a technically complete recovery. Applying sulphuric acid had a great effect on the removal of the aluminium content, as it is shown by the diagrams in *Figure 7*.
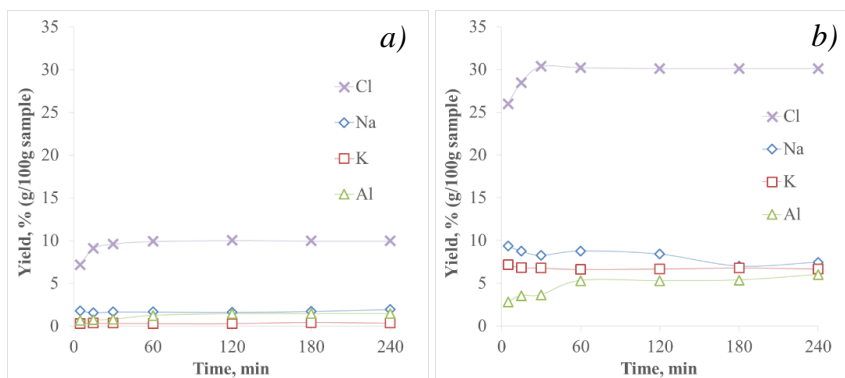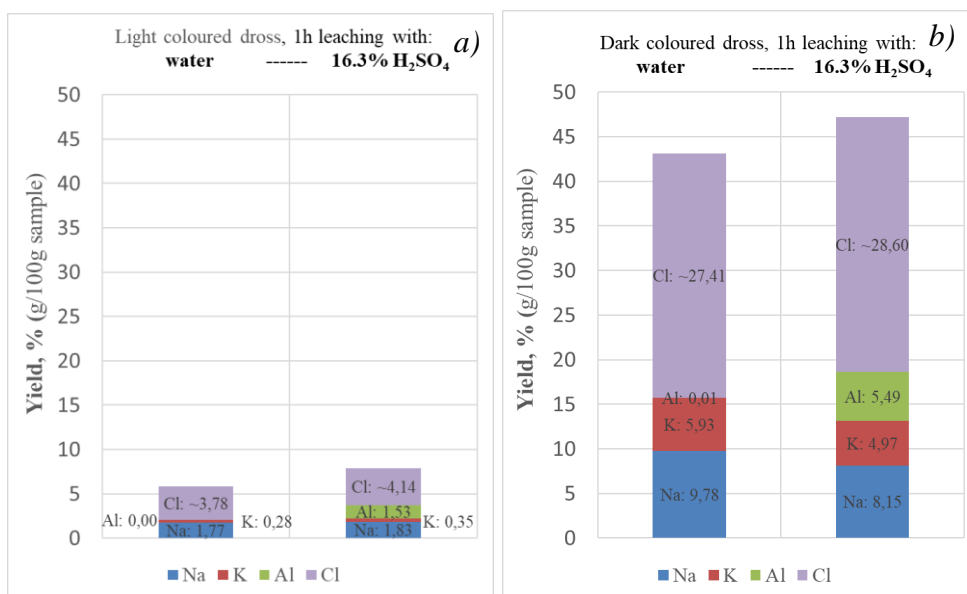

Figure 7

The yields of components by 16.3% H_2SO_4 leaching from (a) the light and (b) dark coloured dross samples obtained from the industrial hot treatment

Based on the AAS analytical results for Na and K, the acid leaching of the light coloured dross gave similar results to those with water, but the acid could remove only ~34% salt relative to the sample mass. This is ~6% lower than that obtained with pure water. On the other hand, the argentometric analysis of the acid leachates gave seemingly higher dissolved chloride results. However, the K_2CrO_4 indicator may be partly converted to the inert H_2CrO_4 form by the acid, causing error. A noticeable change as a result of applying sulphuric acid is the dissolution of ~6% aluminium from the dark dross sample, which was only 1.5% in the case of the light coloured dross. It confirms the assumption that the dross may have received a more aggressive thermal treatment which resulted in a consequently more intensive oxidation, leaving less soluble aluminium in the residual dross. It is shown that the dissolution of the chloride salt content with water is virtually completed in less than 15 minutes, while dissolving Al with the acid may last about four times longer.

2.2. Recovered components

The relative recoveries obtained with water and sulphuric acid in leaching experiments lasting uniformly for 60 minutes are compared in *Figure 8*.

Figure 8

The yields of components by water and 16.3% H_2SO_4 leaching from the light (a) and dark (b) coloured finely ground (<250 µm) dross samples obtained from the industrial thermo-mechanical treatment

The one hour leaching tests could show the total amounts of the practically dissolvable components. Confirming the results of the kinetic study presented in *Figures 6* and *7*, these results also show that the salt content of the dark coloured residual dross

is more than ~5 times higher than that of the light coloured one. However, this ratio is significantly greater for KCl, which is prone to preferential vaporization during high temperatures. It confirms the assumed more aggressive thermal conditions in the case of the preliminary thermo-mechanical treatment producing the light coloured residual dross. The same is the reason for the difference in the dissolved Na/K molar ratios for the two different types of the residual dross (~1.7 in the case of the dark and ~9.3 in the case of the light coloured dross).

Further experiments were carried out to examine the leaching behaviour of residual dross samples obtained by laboratory scale thermo-mechanical treatment [3, 4] of primary melting dross materials originating from the melting of aluminium alloy scrap of negligibly low (<0.1%) and high (~4%) Mg contents, respectively. The results, referring to the 1 hour leaching with either water or 16.3% sulphuric acid, are shown in *Figure 9*. Again, a great difference is seen in the yielded amounts of the dissolved chloride salts, although they were added at the same rate (~10%) to both charges. It shows that a higher loss by evaporation could happen during the thermo-mechanical treatment of the primary dross containing high-Mg aluminium alloy as the entrained metal. The ratio of the more volatile KCl component to NaCl is lower also in this case, indicating the higher temperatures reached as a result of Mg oxidation. These conditions did not reduce the relative amount of the Al metal dissolved by acid leaching, showing that the thermo-mechanical treatment in the induction-type laboratory furnace did not entail higher degree of re-oxidation even at higher temperatures.
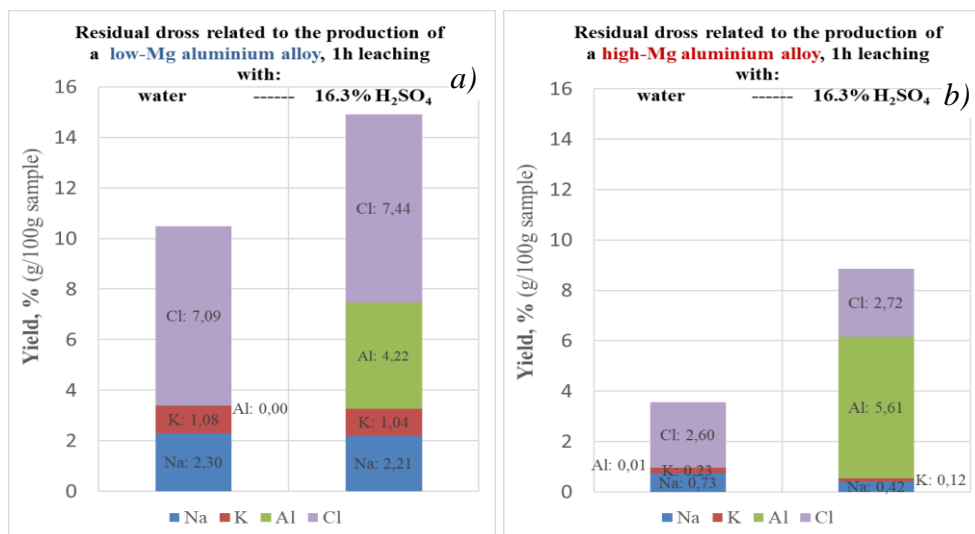
Figure 9

The yields of components by water and 16.3% H₂SO₄ leaching from the residual dross related to the production of low-Mg (a) and high-Mg (b) finely ground (<250 μm) dross samples obtained from the laboratory thermo-mechanical treatment
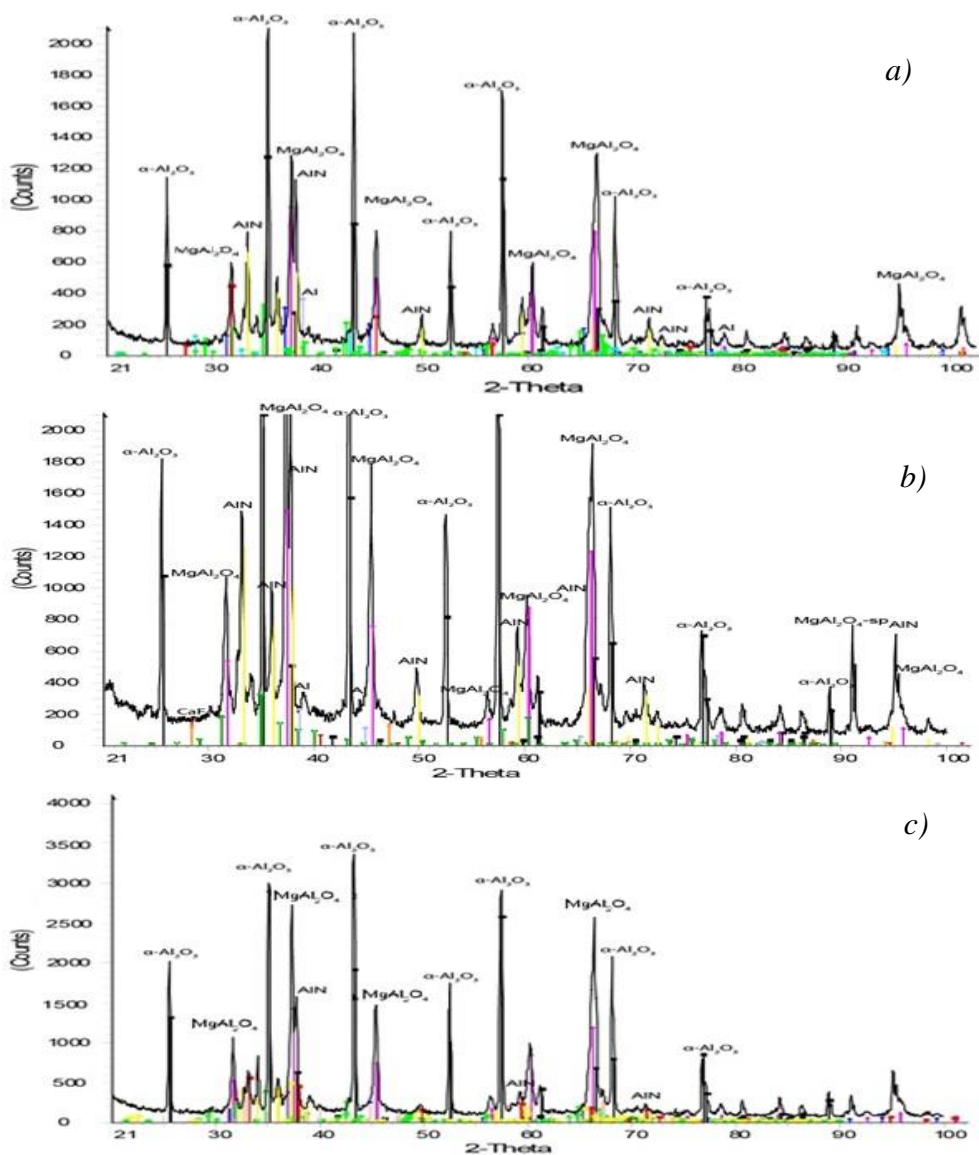
The compositions of the solid residues obtained from the 1 hour leaching experiments were examined – after drying at 105 ºC – by similar instrumental techniques as applied for the raw materials. The SEM images were similar to those of the raw samples in *Figure 3*, but showed more wrinkled surfaces of particles consisting of Al and O, indicating the presence of α-Al_2O_3. The major difference was the missing Na, K and Cl peaks in the relevant EDS spectra, confirming the removal of the salt content by either examined leaching agents. The phases detected after the leaching of the light coloured dross residue with water, H_2SO_4 and – for reference – with NaOH are marked on the XRD spectra of *Figure 10*. Because of the higher initial salt concentration, the effects of leaching can be even more clearly demonstrated by the XRD spectra of the solid residues from the hydrometallurgical treatment of the dark coloured dross sample shown in *Figure 11*. In order to confirm the efficiency of the treatment, these XRD spectra should be compared to those of the starting materials shown in *Figure 4*.

In the solid residue of the light coloured residual dross, α-Al_2O_3 has become dominant, but the presence of $MgAl_2O_4$ spinel is also evident as the water leaching removed the chloride salts. The diffractogram obtained after the sulphuric acid leaching is similar, but the spinel seems to be present at a higher proportion, indicating the higher chemical stability of the $MgAl_2O_4$ compound. The intensity of the AlN peaks are slightly higher when acid was used instead of water for leaching. It shows that the unpleasant evolution of NH_3 may be slightly depressed by the addition of sulphuric acid in the water for leaching the residual dross obtained from the high temperature thermo-mechanical treatment of the primary dross. The remaining – slight – metallic Al content is hidden under a thick oxide cover, which cannot be detected by the X-ray beam of the XRD or the electron beam of the SEM techniques. The leaching with the aggressive 6M NaOH solution could release and dissolve virtually all the metallic Al, but it also involved a strong evolution of gas and heat. Beside the evolution of H_2 from the dissolution of metallic Al, the reaction of AlN with water is enhanced by NaOH according to *Equation (3)*, resulting in a more intensive generation of NH_3. This reaction is evidenced as the AlN peaks are removed after the NaOH leaching.
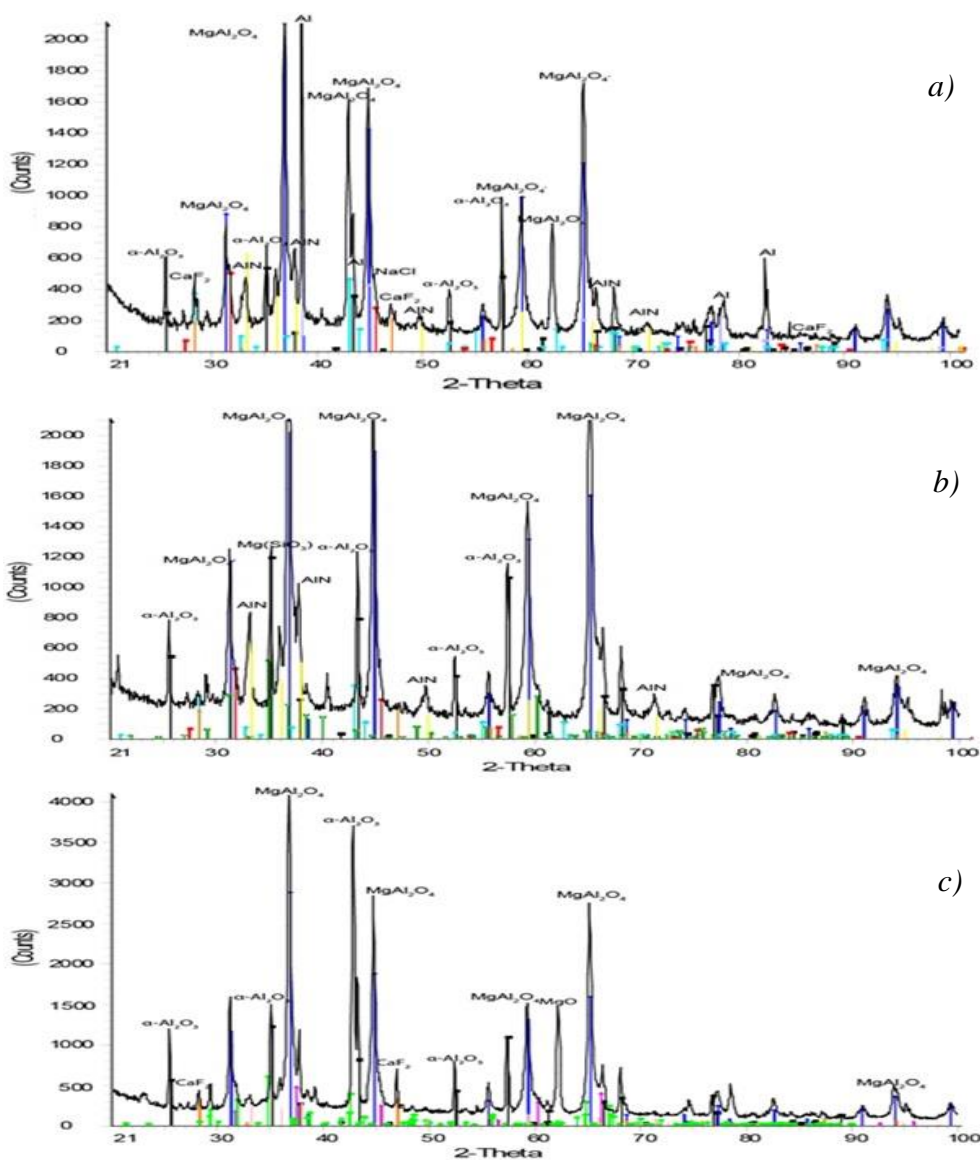
In the solid residue obtained by leaching the dark coloured dross – of high original salt content with water, the spinel $MgAl_2O_4$ and the α-Al_2O_3 compounds were predominant and the metallic Al could also remain beside the relatively lower AlN content. The dominance of the spinel component becomes evident, but also the metallic Al is clearly detected. These characteristics are different from the previous case of the residue from the water leaching of the light coloured dross sample. Due to the probably milder thermal conditions during the preliminary thermo-mechanical processing at the industrial plant, the evaporation of Mg metal and the salt components could be less intensive, and the former could extensively form spinel compounds. The greater salt content could enhance the coalescence of aluminium droplets, which resulted in a decrease of secondary oxidation and cleaner surface of the appearing metallic particles. The relatively higher diffraction peaks of AlN can be seen after the sulphuric acid leaching, indicating again the repression of the harmful reaction (2) by the acidic medium. Metallic Al was already missing from the XRD spectrum obtained from the residue after the acid leaching. The only remaining salt component

was the small amounts of the additive CaF_2, which is not dissolved neither in water nor in the alkaline solution. Experience has shown, that it may be gradually converted to the sulphate by applying sulphuric acid, but a – relatively slight – dissolution of Ca may be noticed only during a subsequent water rinsing.

Figure 10
The XRD spectra of the solid residues of the light coloured finely ground (<250 μm) dross samples obtained from the industrial thermo-mechanical treatment after 1 hour of leaching with water (a), 16.3% H_2SO_4 (b) and 6M NaOH (c)

Figure 11

The XRD spectra of the solid residues of the dark coloured finely ground (<250 μm) dross samples obtained from the industrial thermo-mechanical treatment after 1 hour of leaching with water (a), 16.3% H_2SO_4 (b) and 6M NaOH (c)

2.3. Removal efficiency

The results of the kinetic and the equilibrium studies shown above suggest, that the residue from the thermo-mechanical treatment of the aluminium melting dross may be purified by a suitable hydrometallurgical treatment applying sequential leaching and

washing steps. The most important criterion for any further application of the residue is the elimination of the salt content, however the removal of the metallic phase remaining in the residual dross after the industrial thermo-mechanical processing was also considered. The chloride salts could be dissolved relatively quickly by applying water, and dilute H_2SO_4, was found suitable to dissolve the minor amounts of the metallic components too. In order to establish a workable process, the efficiency of elimination had to be tested by carrying out multiple steps of leaching and subsequent washing, including solid/liquid separations. The efficiency of elimination is shown by the diminishing concentrations in the subsequent leachate solutions.

In this case, a different experimental set-up had to be applied. The ground residue samples – of 300 g – obtained from the industrial thermo-mechanical processing aluminium melting dross of low-Mg alloy scrap were leached with water for 10 minutes in each step and with 16.3% H_2SO_4 for 30 minutes, respectively. The horizontal shaker was run at a high intensity to prevent settling of the finely ground material. The repeated leaching steps were carried out after decanting the clear solution and replacing it with the fresh leaching solution. After the last leaching in the shaking bottles, decanting was followed by simple washing carried out by adding distilled water to the thick sludge after decanting the solution. Washing was repeated in multiple steps separated by decantation. The final washing step was followed by filtering during which distilled water was used to rinse the filter cake. All the steps of this procedure were carried out by the addition of and 500 cm^3 volumes of the leaching solution or washing water. Samples were taken from the decanted solutions for AAS analysis of the dissolved metal concentrations. The yields were calculated to express the amounts of the metals removed by the solution applied at the relevant step relative to the original mass of the treated dross sample. The results of the multi-step leaching with water or dilute H_2SO_4 followed by repeated washing and a final rinsing-filtering are shown in *Figure 12*. The pH values measured in the solutions of the operation applying water are also given.

The total amounts of the removed salt – calculated from the analysed concentrations of Na and K in the solution samples – are approximately the same by applying water or dilute H_2SO_4. However, the acid leaching was carried out for longer time for dissolving also the metals, which resulted in a more efficient leaching of the salt components in the first step too. The alkaline pH of the solutions in water leaching results from reactions (1), (2), which may also be detected by the smell of ammonia gas. Besides the dissolution of metallic components of the dross, minor amounts of dissolved Ca may also appear especially during the water washing steps after the H_2SO_4 treatment, caused by the partial transformation of the CaF_2 component. Dissolved components appearing in the subsequent steps of leaching and washing may have resulted not only from further dissolution, but also from imperfect liquid/solid separation by decantation, leaving significant portions of the previous solution behind in the sludge.
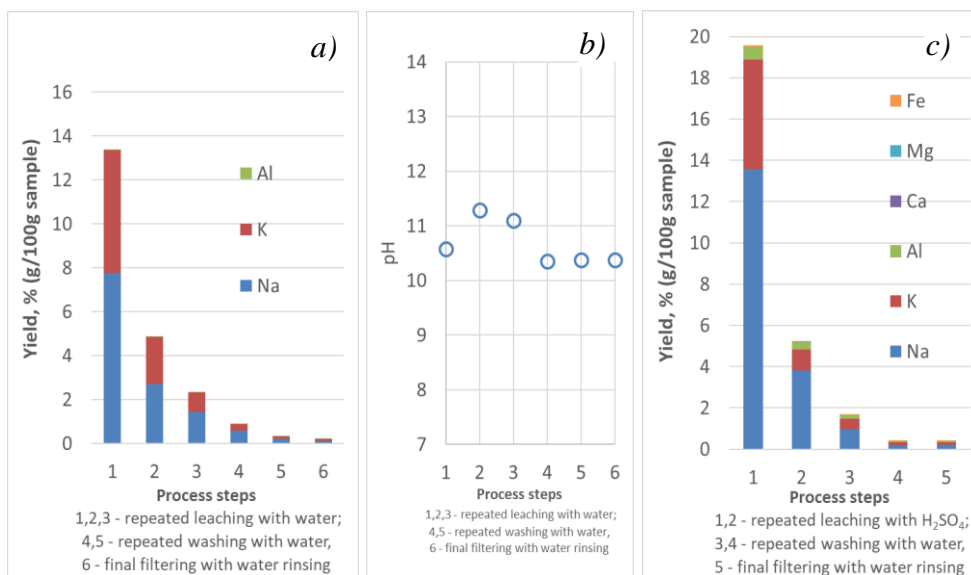
Figure 12
Leaching with water (a, b) or 16.3% H_2SO_4 (c), followed by decanting washing steps and a final filtering rinsing with water rinsing (of different dross samples)

CONCLUSIONS

A relatively simple hydrometallurgical treatment can significantly change the composition and structure of the residual dross obtained from the thermo-mechanical processing of the primary dross generated by melting alloyed aluminium scrap. Water leaching is efficient and quick in removing the chloride salt content. NaCl and KCl are virtually eliminated within a few minutes. The side-reaction of AlN – generated at the high temperature pre-treatment of the dross – with water may also occur. It causes the evolution of some NH_3 gas. Its absorption or collection and combustion should be coupled with any implementation of the aqueous processing of the dross.

Either H_2SO_4 or NaOH solutions are efficient in dissolving not only the chloride salts, but also the remaining metal content in the treated dross, however this process is slower. The generation of NH_3 is repressed by the acid, but strongly intensified by NaOH in the solution.

Water leaching may be sufficient if only the removal of the easily soluble chloride salts is intended, which can be recycled after evaporating the solution. A low concentration of the remaining metallic phase is dispersed in small particles covered by thick oxide layers. If its removal is also required, a second leaching with dilute sulphuric acid should be included. The leaching operation must be followed by sequential washing steps with water and a final filtering. Less washing steps are required if filtering is used instead of decantation for the solid/liquid separation. The solid resi-

due may be utilized in various industrial technologies. Its minor metal content, covered by an oxide layer, is virtually inert, but it may even be beneficial in some applications (like steel making or glass foaming).

ACKNOWLEDGEMENT

REMARK

The content of this paper has been partly presented at the MultiScience XXXIInd MicroCad International Scientific Conference, 5–6 September, 2018, Miskolc, Hungary.

REFERENCES

[1]   Han, Q. et al. (2003). Dross formation during remelting of aluminium 5182 remelt secondary ingot (RSI). *Materials Sci. Eng.*, A363, pp. 9–14.

[2]   Krone, K. (2000). *Aluminium Recycling*. Düsseldorf: VDS.

[3]   Tóth, G. B., Harangi, Z., Kulcsár, T. & Kékesi, T. (2013). Metal content of drosses arising from the melting of aluminium, in Proceedings of the *XXVIIth MicroCad International Scientific Conference*, Miskolc, Hungary, March 21–22, 2013, Section C-D/14, p. 12.

[4]   Kékesi T. & Kulcsár T. (2017). Ötvözött alumíniumhulladékok olvasztása során keletkező salakok jellemzői. *BKL-Kohászat*, 150, 1, pp. 23–29.

[5]   Ho, F. K. & Sahai, Y. (1990). Interfacial Phenomena in Molten Aluminium and Salt System. *In Proceedings of the 2nd Int. Symp. Recycling of Metals and Engineered Materials*. van Linden, J. H. L., Stewart, D. L., Sahai, Y. (eds.). Warrendale: TMS, pp. 85–103.

[6]   Peterson, R. D. (2011). A historical perspective on dross processing. *Materials Science Forum*, Vol. 693, pp 13–23.

[7]   Xiao, Y., Reuter, M. A. & Boin, U. (2005). Aluminium Recycling and Environmental Issues of Salt Slag Treatment. *Journal of Environmental Science and Health*, 40, pp. 1861–1875. http://www.ips-engineering.net/Doc/Engitec/STE%20Process.pdf [Accessed Aug. 10. 2018].

[8]   Liu, Y. et al. (2014). Study on hydrometallurgical process and kinetics of manganese extraction from low-grade manganese carbonate ores. *International Journal of Mining Science and Technology*, 24, 4, pp. 567–571.

[9]   Bar, D. L. & Barket, D. (2015). The leaching of sulfide iron (II) with sulfuric acid. *Journal of Mining Science*, 51, 1, pp. 179–185.

[10] Gilchrist, J. D. (1979). *Extraction Metallurgy*. 2nd Rev Ed, Oxford/New York: Pergamon Press.

THE STRENGTH PROPERTIES INVESTIGATION
OF CHEMICALLY BONDED SAND MIXTURES

HENRIETTA HUDÁK[1]–LÁSZLÓ VARGA[2]

Foundry technology use a lot of several natural materials. Sands use for preparing mixtures whereby making moulds or cores. Sand is defined as granular, refractory major portion of mixture (90–98% in dependence on used binder). Sand properties depend on it has chemical and mineralogical composition; mainly particle-size distribution and shape of grains and it size and sand surface texture. A comparative measurement of two quartz sands with different surface quality was carried out. Chemically bonded sand mixtures were prepared to measure their bending strength. The strength of sand mixtures has two main components. One of them is the cohesion of the binder; the other one is the adhesion between the binder and the foundry sand. The aim of this research is to determine the ratio of cohesion and adhesion within the strength values.

Keywords: sand mixture, bending test

INTRODUCTION

Several types of sands are used for moulding and core making. Quartz sand is the most frequently applied type of foundry sands not only because of its widespread use but also due to its low price. The quality of quartz sand determines the physical and chemical properties (e.g. grain size, shape, grain-size distribution, chemical composition, refractoriness). Based on the source materials, the sand core test specimens made of different surface quartz sands show even a double difference in their bending stress values [1–4].

Sands of almost the same granulometric but different micro surface properties can show variable behaviour in respect of the foundry use. The micro surface of the sands plays a very important role in the requirement for binders. Saving in the binder can be reached – achieving, however, the same strength, when choosing smooth surface sand [5].

Quartz sand of two different surfaces was used for our tests (GBM 45 and SH 33). *Figure 1* shows the grain morphology of different sands while a grain size distribution of them can be seen on *Figure 2*.
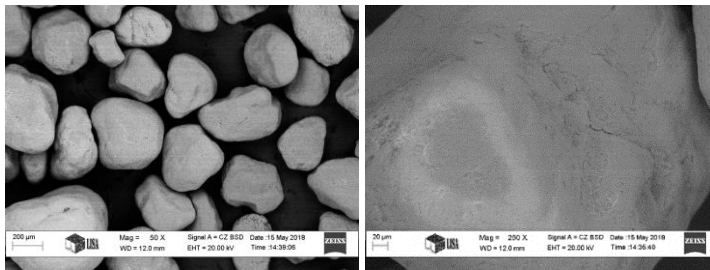
---

[1] Institute of Foundry, University of Miskolc
   H-3515 Miskolc-Egyetemváros, Hungary
   ontheni@uni-miskolc.hu

[2] Institute of Foundry, University of Miskolc
   H-3515 Miskolc-Egyetemváros, Hungary
   ontvlaci@uni-miskolc.hu
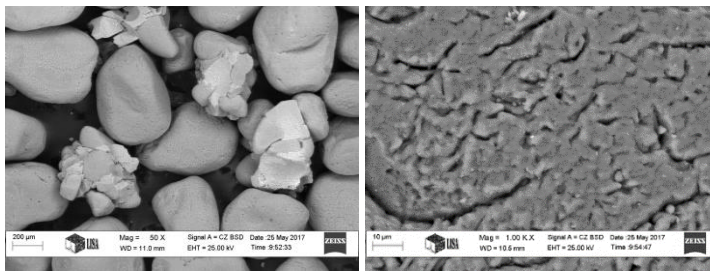
a)

b)

Figure 1
Scanning electron microscopy (SEM) image of quartz sands.
   a)   GBM 45 (N = 50x) and (N = 1000x).
   b)   SH 33 (N = 50x) and (N = 250x).
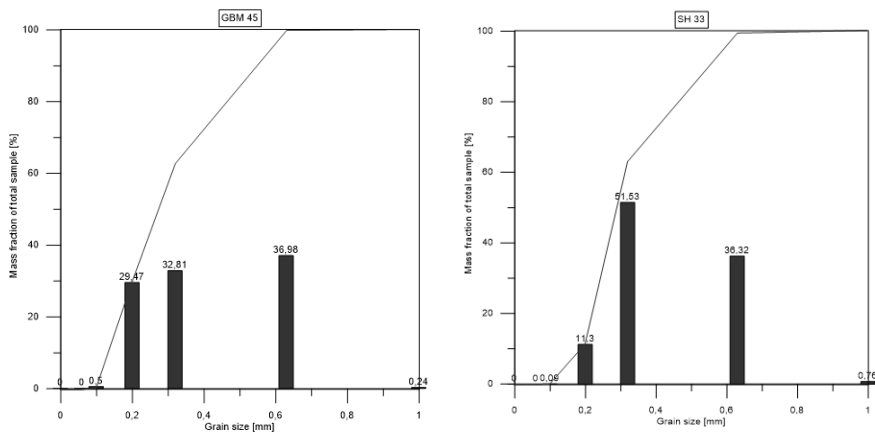
Figure 2
Grain size distribution of the used quartz sands

After the granulometry analyses we compared two types of determination of the specific surface. Here are several methods to measure or estimate the surface area. The most widely used method in the foundry industry is the Blaine measurement. The air

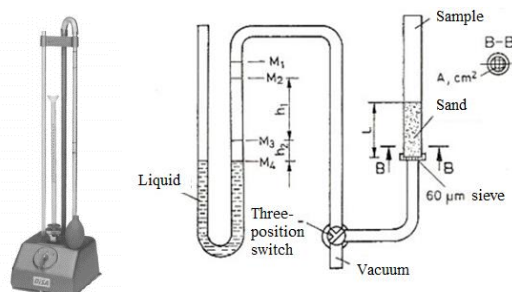permeability test was performed according to the method described in the Foundry Standard.

Figure 3
Types of DISA Blaine Air Permeability Apparatus and the measure method

The other one is BET technique, is based on the adsorption of a monolayer of gas, in our case nitrogen, on the surface of particles. The total surface area of a powder can be calculated using the Langmuir theory and the BET generalization.
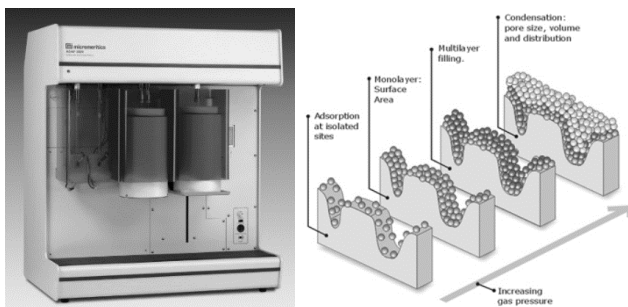
Figure 4
Micromeritics ASAP 2020 Surface Area Analyser and the measurement method

Table 1
Measurement data of the investigated sands

	GBM 45	**SH 33**
Average granularity (d_{50})	0.303 mm	0.333 mm
AFS granularity number	61.7	51.9
Homogeneity degree	44 %	58 %
Angularity coefficient of sand	1.14	1.24
Specific surface (A_{BLAINE})	*90 cm^2/g*	*110 cm^2/g*
Specific surface (A_{BET})	*520 cm^2/g*	*900 cm^2/g*

We compared two methods for determination of the specific surface. Correlation between BET and the Blaine methods was not good. Measured specific surface area by the BET method was always higher than results come from Blaine measurement. The difference between the surface areas measured by Blaine and BET could be attributed to the porosity and surface roughness of the particles.

The *Figure 5* shows the determination of the method for cohesion and adhesion.

Figure 5

The method used for determining the cohesion and adhesion

Different resin binding sand mixtures were made from different type of sands. Sand were added to mixtures **with and without fractionation and grain sizes were fine, medium and coarse.** Binder quantity and quality were the same to ensure an equal number of the bond bridges which are the connection points of the sand grains.

Specimens for bending strength were prepared with **hot-box technology** where baking temperature and shooting pressure were identical.

The ratio of cohesion and adhesion can be determined from the strength value results. In case of different surface qualities of samples with identical size distribution and binder quantity, equal bond strength developed. This means that the cohesion between sand grains was nearly the same. The difference between strength values may arise from the difference in the adhesion, which depends on the surface quality of the sand grains.

1. EXPERIMENT

Core sand mixtures were made within average laboratory environment. The quantity of the resin (Thermophen) was 1.5% and the quantity of the catalyst (Haerter) was 0.30%, respectively to the quantity of the sand. The mixture was prepared with a laboratory mixer, within 2 minutes of mixing time (resin –1 minute and catalyst 1 minute).

Core sand mixture was shot into the preheated (220 °C) core box with the Multi-serw-Morek core shooter (3 bar pressure), and after 50 seconds of baking time, the specimens used for bending strength were created (standard size 22.5 mm × 22.5 mm × 185 mm).

1.1. Bending strength

This measurement gives information about the bond strength of the standard specimen. A three-point bending test specimens have to be put on the machine two supports (according to the VDG-testing standard P72.) at 150 mm distance from each other. At the midpoint of the speciment will be loaded with evenly increasing force until breaking. Bending strength measurements were carried out immediately, after 1 and 24 hours, after the core shooting.

Bending strength ($\sigma_{bending}$ [N/cm^2]) can be calculated with the following formula:

$$\sigma = F \cdot \frac{3l}{2a^3} \tag{1}$$

where: F – is the loading force [N]
                       l – is the distance of the two supports [mm]
                       a – is the side length of the specimen [mm] [6].

2. RESULTS

Table 2 shows the bending test results of different sand mixtures.

<div align="right">

Table 2
The bending test results

</div>

	Bending strength [N/cm^2]		
	Instantly	1 hour	24 hour
SH 33 without fractionation	*254.37*	*228.93*	*208.23*
GBM 45 without fractionation	*351.83*	*322.37*	*280.60*
SH 33 Fine fraction (110-220 μm)	*204.03*	*203.13*	*170.50*
GBM 45 Fine fraction (110-220 μm)	*307.47*	*264.67*	*248.83*
SH 33 Medium fraction (220-300 μm)	*260.80*	*245.40*	*220.40*
GBM 45 Medium fraction (220-300 μm)	*329.20*	*306.33*	*249.77*
SH 33 Coarse fraction (300-540 μm)	*283.87*	*273.07*	*216.83*
GBM 45 Coarse fraction (300-540 μm)	*360.23*	*352.13*	*278.80*

The results of bending tests are illustrated on *Figures 6–9*. The *Figure 6* shows the bending test results of the sand mixtures without fractionation. (The illustrated measurement results come from the average of the 3 measurements.)
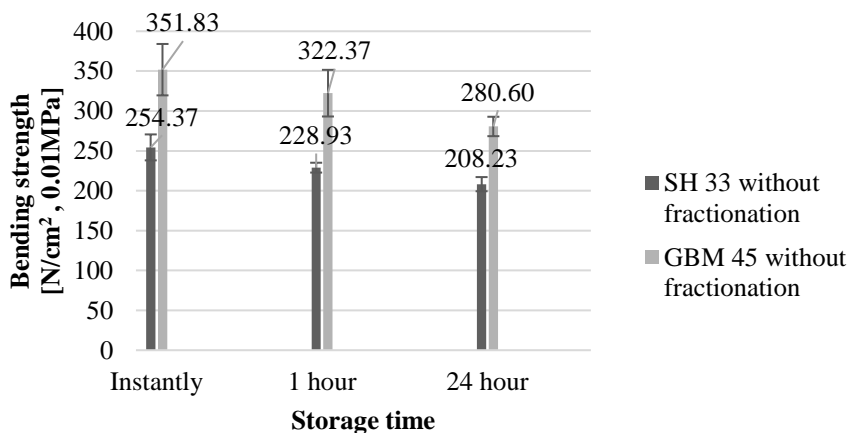
Figure 6
Bending test results – without fractionation

Figure 6 can be seen that the measured strength of the specimens made of quartz sand type GBM 45 (even in case of without fractionation) is higher than that of the specimens made of SH 33 type sand.

The *Figures 7–9.* illustrate the bending test results of the sand after fractionation. (The illustrated measurement results come from the average of the 3 measurements.)
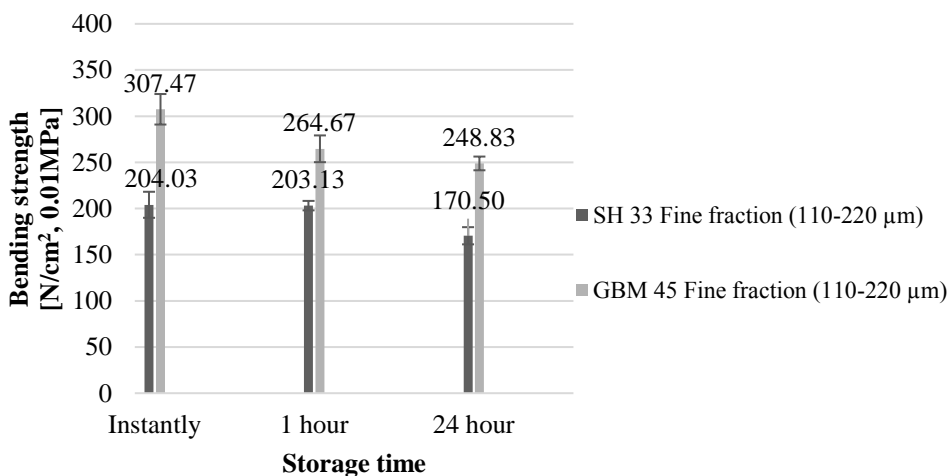
Figure 7
Bending test results – fine fraction
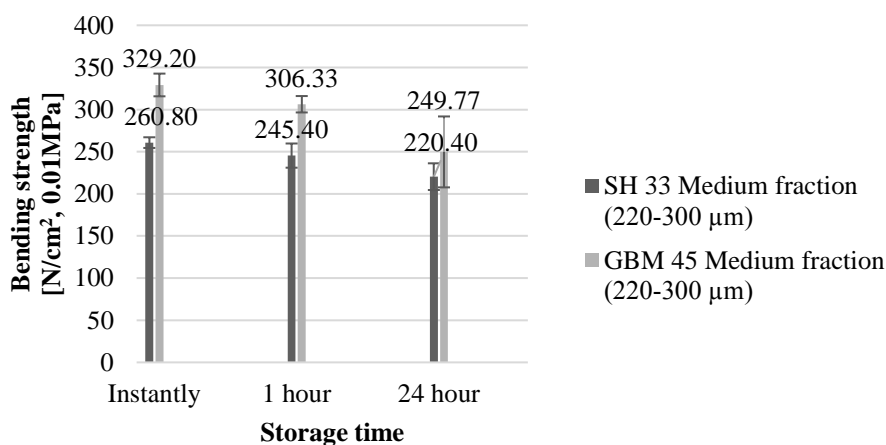
Figure 8
Bending test results – medium fraction
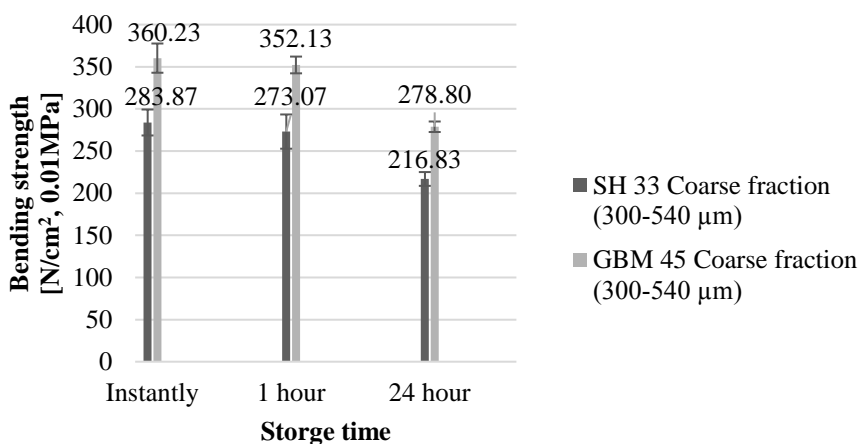
Figure 9
Bending test results – coarse fraction

Based on the results of the bending strength *(the Figures 7–9)*, it can be seen that the measured strength of the specimens made of quartz sand type GBM 45 (even in case of different fractions) is higher than that of the specimens made of SH 33 type sand. *Figure 10* shows all of the measured bending strength results as the function of the storage time.
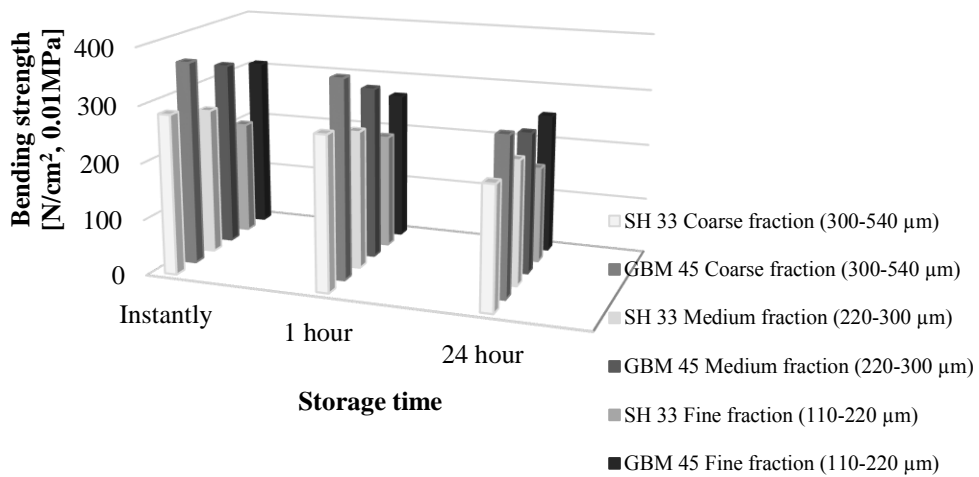
Figure 10
Bending test results – all of fraction

Bending strength values of the specimens made of rough fraction sands are higher than those of fine fraction - in case of both types of sand.

Figure 11 demonstrates the immediate bending strength values, as the discrepant fractions of the different sands.
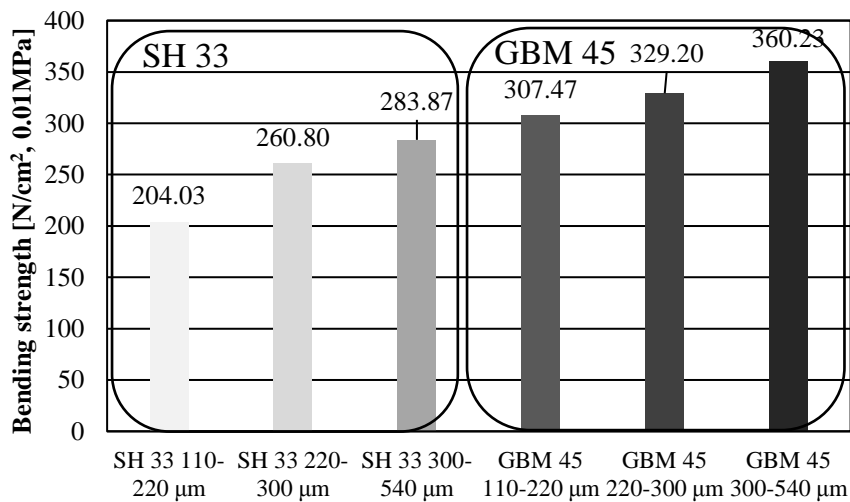
Figure 11
Immediate bending test results

In consequence of by the demonstrating the immediate bending strength values of the different sands, a discrepancy can be seen between the cohesion. Change in cohesion values can be explained by different granulometric properties, characte-ristic of bond bridges and the number of the binding points.

Figure 12 shows scanning electron microscopy images of broken specimen surfaces.

a)   b)
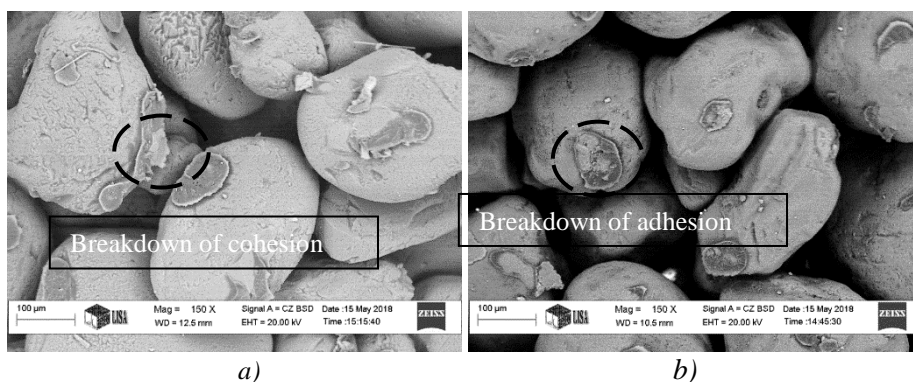
Figure 12

Scanning electron microscopy (SEM) images of broken surface of the specimens.
a)   GBM 45 (N = 150x).
b)   SH 33 (N = 150x).

The nature of destruction can be seen well in the images of the two different quartz sands. Cohesion and adhesion breaks can be distinguished.

SUMMARY

We compared two types of determination of the specific surface for foundry sands. Correlation between BET and the Blaine methods was not good found.

And then, we prepared chemically bonded sand mixtures to measure their bending strength. The results of the investigation show that foundry sands with different micro surfaces can have different binding strength values. With the help of the fractionation method of the sand grains, the cohesion and adhesion ratio can be determined from the measured strength values.

ACKNOWLEDGEMENT

REMARK

The content of this paper has been partly presented at the MultiScience XXXIInd MicroCad International Scientific Conference, 5–6 September, 2018, Miskolc, Hungary.

REFERENCES

[1]   Löchte, K. (1998). Working with the Cold Box Process in the Coremaking Department of a Foundry. [Online].

[2]   Bechný,V. (2012). Zukünftige Herausforderungen an Gießereisande. *Giesserei-Rundschau*, Vol. 59, No. 3, pp. 81–83.

[3]   Iden, F., Tilch, W., Wojtas, H. J. (2011). Die Haftungsmechanismen von Cold-Box-Bindemitteln auf der Formstoffoberfläche. *Giesserei*, 5, pp. 24–36.

[4]   Iden, F., Pohlmann, U., Tilch, W., Wojtas, H. J. (2011). Strukturen von Cold-Box-Bindersystemen und die Möglichkeit ihrer Veränderung. *Giesserei Rundschau*, Vol. 58, No. 1, pp. 3–8.

[5]   [Online] http://giba.at/pdf/giba-de.pdf

[6]   *Öntészeti Szabványok.* II. kötet, Szabványkiadó, 1977.

SHORT OVERVIEW OF MULLITE BASED CERAMIC COMPOSITES REINFORCED WITH SILICON-CARBIDES

EMESE KUROVICS[1]–SERGEI KULKOV[2]–LÁSZLÓ A. GÖMZE[3]

In this research the roles of mullite in the technical ceramics and ceramic matrix composites were examined by the authors. On the basis of the analyzed research papers it was found that the silicon carbide (SiC) whiskers and particles can considerable increase the mechanical strengths and toughness of the mullite based ceramic composites.

Keywords: ceramic, composite, mullite, silicon-carbide

INTRODUCTION

In the last 10–15 years the industry, environment safety as well as life science are requirednew, low density materials with increased physical, electrical, magnetic, mechanical, thermal or chemical properties. Thanking to these increased requirements to properties more and more ceramic materials and ceramic based composites are developed and used in different areas of industry and technology [1], [2], [3], [4], [5], [6], [7], [8], [9], [10], [11], [12], [13], [14], [15], [16].

At the same time the final physical, chemical or biological properties of the developed new materials are very strong depended both on the used raw materials, technological know-how and processes [18], [19], [20], [21], [22], [23], [24], [25], [26], [27].

Comparing with high-performance light metals and metal alloys even the oxide ceramics have much higher mechanical strengths, hardness, module elasticity and melting temperatures [17], [28], [29], [30], [31], [32]. Generally, the non-oxide ceramics like AlN, TiN, ZrN or Si_3N_4 and SiAlON reinforced corundum matrix composites have higher melting temperatures and elasticity modulus than the oxide ceramics [33].

In our days from the technical ceramics the highest module of elasticity has the WC meanwhile the highest melting temperatures have the TaC and HfC. From the *Figure 1* it is obvious that the non-oxide technical ceramics and carbide ceramics have much higher surface hardness and compression strengths than metals and metal alloys or oxide ceramics, but in many cases their production costs are very expensive. Mostly to produce non-oxide and carbide ceramics very fine grain size powders are

[1] Department of Ceramics and Silicate Engineering, University of Miskolc
   H-3515 Miskolc-Egyetemváros, Hungary
   fememese@uni-miskolc.hu
[2] Institute of Strength Physics and Materials Science SB RAS
   Akademicheskiy Prospekt, 2/4, Tomsk, Tomskaya oblast, Russia
[3] Department of Ceramics and Silicate Engineering, University of Miskolc
   H-3515 Miskolc-Egyetemváros, Hungary
   femgomze@uni-miskolc.hu

used and their heat treatments (sintering processes) are done in vacuum or in inert gas at temperature of 2,000 °C or higher. Our aims are to develop ceramic composites with increased physical and mechanical properties using relatively not expensive processing technology and raw materials like conventional kaolinite or other clay minerals. The conventional kaolinite and alumina-hydro-silicates are widely used in traditional ceramic industry and its thermal dissipation is well known both from literature and practice *(Figure 2)* [34], [35], [36], [37].
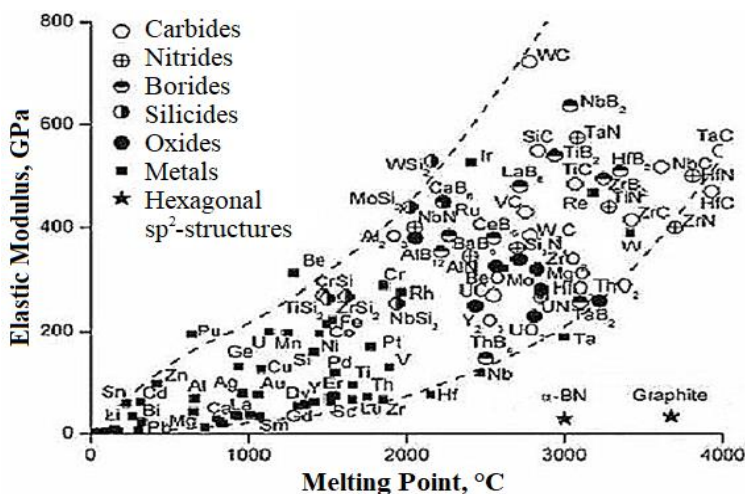
Figure 1
The relation between melting point and elasticity modulus of different materials
[17] (Taken from Gömze, L. A., Gömze, L. N. 2017)
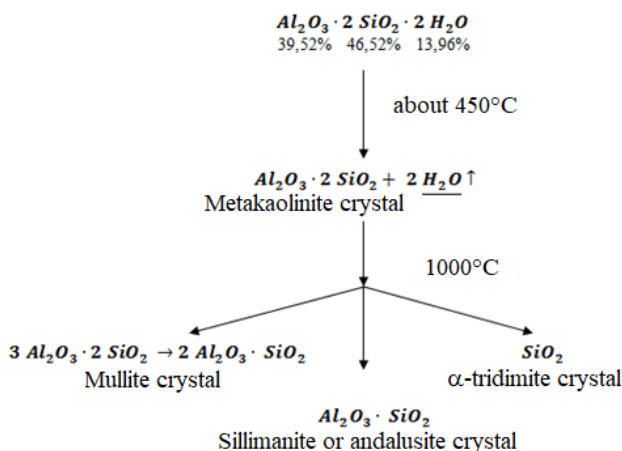
Figure 2
Thermal decomposition of kaolinite crystals
(Taken from Ceramic Yearbook I. 2001 [34])

1. MULLITE AS IMPORTANT CERAMIC INGREDIENT

Mullite is a stable intermediate phase of the Al_2O_3-SiO_2 system under atmospheric pressure, which does not occur in large quantities as minerals in the nature in spite that it is one of the major components of the sintered traditional ceramics like potteries, stoneware, porcelains or fireclays. In high-temperature burned (sintered) ceramics (for example in hard porcelains), there are two characteristic morphologies of mullites can be found: the primary or alumina rich 2 : 1 mullite (**$2Al_2O_3 \cdot SiO_2$**) which has a flake structure and secondary or silicon rich 3 : 2 mullite (**$3Al_2O_3 \cdot 2SiO_2$**) which has needle shapes aggregates (*Figure 3*) [38].
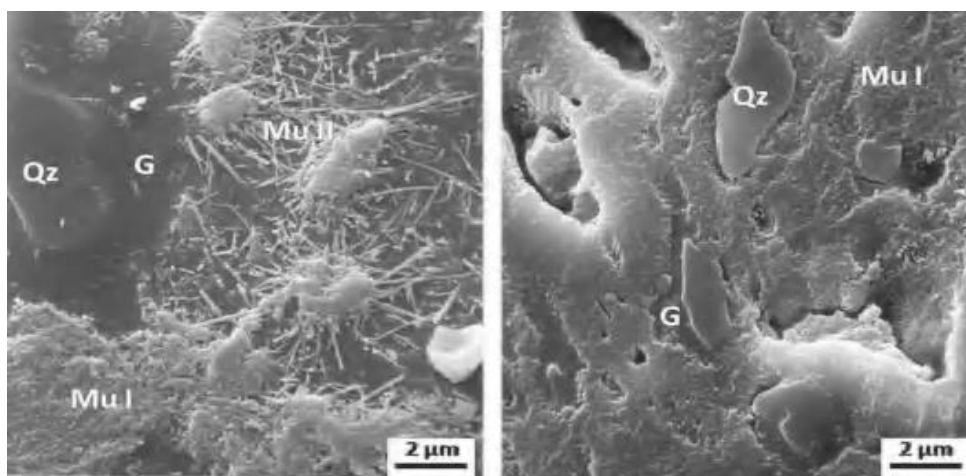
Figure 3
Primary 2 : 1 (Mu I) and secondary 3 : 2 (Mu II) mullite [39]
(Taken from Heimann, R. B.: Classic and Advanced Ceramics, 2010)

The phase diagram of Al_2O_3-SiO_2 system has been studied by many researchers but most of them represent the phases only above 1,400 °C [35], [36], [37]. There are also several scientific works where we can find phase diagram at lower temperatures. For example Berezhny is one of them who have studied and described the phase diagram of Al_2O_3-SiO_2 system from 0 °C at normal (atmospheric) pressure *(Figure 4a)* in the book of Bobkova [36].

The phase diagram of Berezhny shows that the melting point of pure mullite ($3Al_2O_3 . 2SiO_2$) is 1870 °C. It is higher than in the melting temperature of solid mix from mullite and corundum (1,840 °C). The diagram shows very well the various modifications of mixed crystals and how the phases are depending on the temperature. Depending on pressure we can get a quite different phase diagram of the Al_2O_3-SiO_2 system. For example using hot isostatic pressing under 2,500 MPa pressure the $Al_2O_3 \cdot SiO_2$ crystals from sillimanite will be turned into dense kyanite crystals *(Figure 4b)* [36].

(a)   (b)
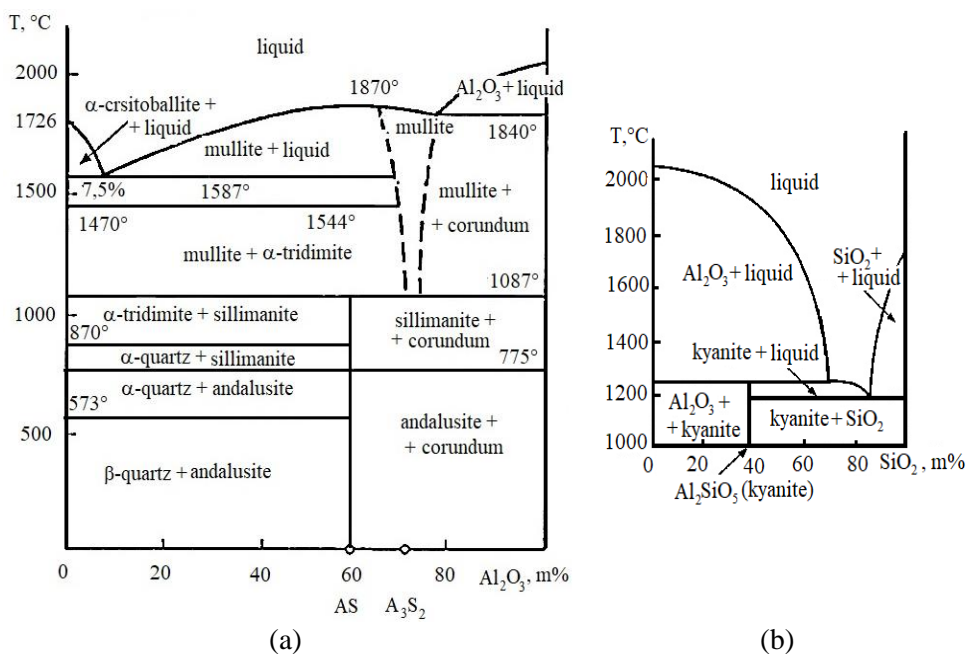
Figure 4
SiO₂-Al₂O₃ system at normal (a) and at 2,500 MPa pressure (b) [36]
(Taken from Bobkova, N. M.: Fizicheskaya Himiya Tugoplavkih
Nemetallicheskih i Silicatnyh Materialov, 2007)

Generally at normal (atmospheric) pressure the mullite crystals are capable to incorporate a number of transition metal cations and other foreign atoms into their structures depending on sintering environment and temperature [34], [36], [37], [38]. Thanks to these excellent thermo-chemical properties of mullite crystals a wide range of light weight ceramic reinforced hetero-modulus, hetero-viscous and hetero-plastic composites could be developed in the last 8–10 years [5], [7], [20], [31], [39], [40], [41], [42].

Despite the rare occurrence of mullite as mineral, the sintered mullite crystals are playing important role both in traditional and modern technical ceramics. Due to the excellent mechanical strengths in high temperature and chemical stability the mullite ceramics have great technical significance not only in the refractory materials industry. For example in Russia the significant part of their refractory accessories are made from melted mullite with 25–27 m% of SiO_2 content [36]. Comparing with the ZrO_2 the $3Al_2O_3 \cdot 2SiO_2$ mullite has relatively same or higher toughness, only half of linear thermal expansion and about 56% in weight (density) *(Table 1).*

Thermo-mechanical properties of mullite and other oxide ceramics [38]

Properties	Spinel	α - Aluminum oxide	Zirconia	Mullite
Composition	$MgO \cdot Al_2O_3$	Al_2O_3	ZrO_2	$3Al_2O_3 \cdot 2SiO_2$
Melting point, °C	2,135	2,050	2,600	≈1,830
Density, g/cm^3	3.56	3.96	5.6	≈3.2
Linear thermal expansion, $\cdot 10^{-6}\,°C^{-1}$, 20–1400 °C	9	8	10	≈4.5
Mechanical strength, MPa	180	500	200	≈200
Fracture toughness K_{IC}, $MPam^{0,5}$	–	≈4.5	2.4	≈2.5

(Taken from Schneider, H. et al.: Structure and properties of mullite – A review, 2008)

In our days the following 3 types of mullite ceramics are produced: monolith mullite bulks, mullite coatings and mullite matrix composites [38], [43]. By Vakalova and her co-authors was found out the mechanism of activation of mullite synthesis in rusk kaolinite at temperature range 1,100–1,400 °C. Adding to the kaolinite powders Fe_2O_3 and MnO_2 components during sintering a formation of interstitial solid solutions of the cations Mn^{4+} (Mn^{2+}) and Fe^{3+} in the lattice of mullite (synthesized from kaolinite) was observed [44]. Thanking to the interstitial solid solution these cations the mechanical strengths of the samples have increased from 72 MPa to 97 MPa *(Figure 5)*.
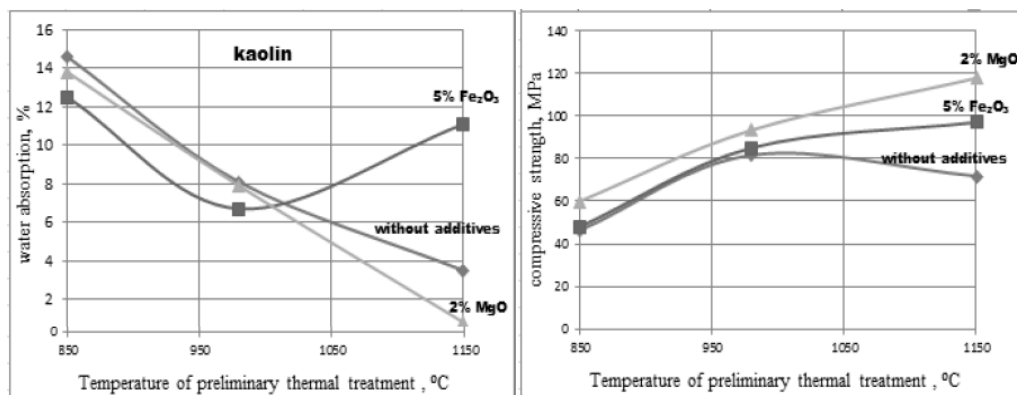
Figure 5
The effect of mineralizing oxides on kaolin [44]
(Taken from Vakalova, T. V. et al.: Activation of Synthesis and
Sintering of Mullite, 2014)

2. SiC REINFORCED MULLITE CERAMICS

There are several methods to produced ceramic matrix nanocomposites [45]. The main goal of development SiC reinforced mullite based ceramic matrix composites is the improvement of toughness. For example, Carter and his co-authors [46] have shown how the volume of silicon carbide whiskers influences on the toughness of different ceramic composites *(Figure 6)*, meanwhile Gustafsson and his co-authors have described how the SiC components prevent the diffusion creep of mullite based nanocomposites [47].
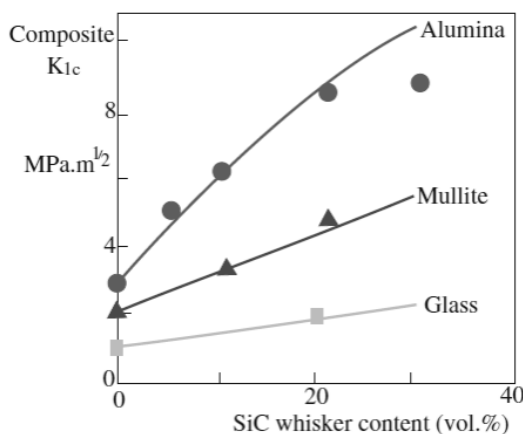
Figure 6
Effect of the amount of SiC whisker for toughness for different matrix materials
[46] (Taken from Carter, C. B., Norton, M. G.: Ceramic Materials Science and Engineering 2013)

Y. Sakka already in 1995 described in his work [48] the possible formation of silicon carbide-mullite-alumina nanocomposites through colloidal consolidation and reaction sintering *(Figure 7)*.
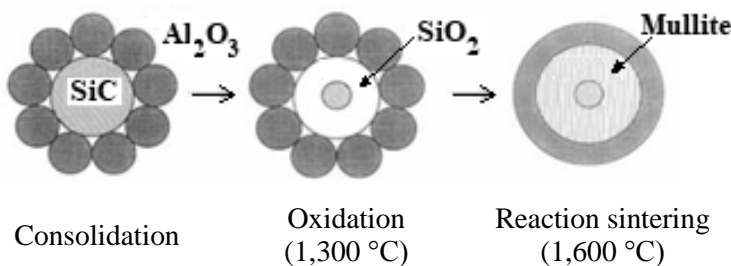
Figure 7
Schematic illustration of nanocomposite production steps [48]
(Taken from Sakka, Y.: Silicon Carbide-Mullite-Alumina Nanocomposites 1995)

Lin and his co-authors have prepared first the mullite based ceramic matrix using sol-gel methods and after have mixed SiC whiskers to them and compacted the mixtures in graphite dies during 20 minutes by hot pressing (HP) at 1,400 °C and 34.5 MPa in argon gas. The produced ceramic composite specimens had 30 m% SiC whiskers and the mullite based matrix material had 32.4 m% ZrO_2 and 2.2 m% MgO. The prepared specimens were tested on oxidation through 1,000 hours at 1,000–1,350 °C [49]. 12 years later Akpinar and his colleges have found that the rheological properties of the aqueous ceramic suspension can be considerable improved by adding 20 m% silicon carbide particles (SiCp) to the suspension. Thanks to the involved SiC particles the firing shrinkage of such prepared specimens during sintering have decreased from 17.5% to 5% [50]. The charitable influence of ZrO_2 particles on mechanical strengths of the mullite content traditional ceramics also was verified in work [15].

CONCLUSION

Summarizing the studied literatures we can say that mullite or mullite containment taken from kaolinite can be successfully used as matrix material for silicon carbide particles or whiskers reinforced ceramic composites. The SiC particles and whiskers can considerable increase the mechanical strengths and toughness of both the kaolinite and mullite based ceramic composites.

ACKNOWLEDGEMENTS

REMARK

The content of this paper has been partly presented at the MultiScience XXXIInd MicroCad International Scientific Conference, 5–6 September, 2018, Miskolc, Hungary.

REFERENCES

[1] Kulkov, S. & Savchenko, N. (2008). Wear behavior of zirconia-bazed ceramics under high-speed dry sliding on steel. *Építőanyag – JSBCM,* 60 (3), 62. http://dx.doi.org/10.14382/epitoanyag-jsbcm.2008.10

[2] Lukin, E. S., Makarov, N. A., Kozlov, A. I., Popova, N. A., Anufrieva, E. V., Vartanyan, M. A., Kozlov, Yu. A., Safina, M. N. & Lemeshev, D. O. (2008). Oxide ceramics of the new generation and areas of application. *Glass and Ceramics,* Vol. 65, No. 9–10, pp. 348–352.

[3]   Morikawa, A., Suzuki, T., Kikuta, K., Suda, A. & Shinjo, H. (2009). Improvement of OSC performance for CeZrO$_4$ solid solution with Al$_2$O$_3$ diffusion barrier. *Építőanyag – JSBCM,* 61 (1), p. 2. http://dx.doi.org/10.14382/epitoanyag-jsbcm.2009.1

[4]   Ershova, N. I. & Kelina, I. Y. (2009). High-temperature wear-resistant materials based on silicon nitride. *Építőanyag – JSBCM,* 61 (2), p. 34. http://dx.doi.org/10.14382/epitoanyag-jsbcm.2009.6

[5]   Gömze, L. A. & Gömze, L. N. (2009). Alumina-based hetero-modulus ceramic composites with extreme dynamic strength – phase transformation of Si3N4 during high speed collisions with metallic bodies. *Építőanyag – JSBCM,* 61 (2), 38. http://dx.doi.org/10.14382/epitoanyag-jsbcm.2009.7

[6]   Rocha-Rangel, E., Hernández-Silva, D., Terés-Rojas, E., Martines-Franco, E. & Diaz-De La Torre, S. (2010). Alumina-based composites strengthened with titanium and titanium carbide dispersions. *Építőanyag – JSBCM,* 62 (3), p. 75. http://dx.doi.org/10.14382/epitoanyag-jsbcm.2010.15

[7]   Gömze, L. A. & Gömze, L. N. (2011). Hetero-modulus alumina matrix nanoceramics and CMCs with extreme dynamic strength. *IOP Conf. Ser.: Mater. Sci. Eng.,* 18, 082001. http://dx.doi.org/10.1088/1757-899X/18/8/082001

[8]   Takato, M., Kaneko, M., Nishi, T., Saito, K. & Uchikoba, F. (2013). Multilayer magnetic circuit for millimeter scale MEMS air turbine generator. *IOP Conf. Ser.: Mater. Sci. Eng.,* 47, 012015. http://dx.doi.org/10.1088/1757-899X/47/1/012015

[9]   Yu, C., Deng, C., Yuan, W. & Zhu, H. (2013). The Effect of Adding TiO$_2$ on Synthesis of Al$_4$SiC$_4$ powders. *IOP Conf. Ser.: Mater. Sci. Eng.,* Vol. 47, p. 012059. http://dx.doi.org/10.1088/1757-899X/47/1/012059

[10] Li, J., Yuan, W. J., Deng, C. J. & Zhu, H. X. (2013). The Effect of Si contents on the reaction-bonded Si$_3$N$_4$/SiC composite ceramics. *IOP Conf. Ser.: Mater. Sci. Eng.,* Vol. 47, p. 012060. http://dx.doi.org/10.1088/1757-899X/47/1/012060

[11] Vereschaka, A., Kutin, A., Sitnikov, N., Oganyan, G., Sharipov, O. (2016). Research of mechanical and cutting properties, wear and failure mechanisms of nanostructured multilayered composite coating Ti-TiN-(NbZrAl)N. *Építőanyag – JSBCM,* 68 (3), p. 114. http://dx.doi.org/10.14382/epitoanyag-jsbcm.2016.20

[12] Torres-Cadenas, S., Bravo-Patiño, A., Zarate-Medina, J., Contreras-García, M. E. (2017). Nest-like BaO•6Fe$_2$O$_3$ microspheres with hierarchical porous structure for drug delivery. *Építőanyag-JSBCM,* 69 (1), p. 2. http://dx.doi.org/10.14382/epitoanyag-jsbcm.2017.1

[13] Tariq, F., Rafique, U., Yaqoob, K. (2017). Synthesis of alumino-silicates functionalized titanium as potential adsorbent: An industrial possibility. *Építőanyag – JSBCM,* 69 (3), p. 94. https://doi.org/10.14382/epitoanyag-jsbcm.2017.16

[14] Kurovics, E., Shmakova, A., Kanev, B. & Gömze, L. A. (2017). Development ceramic composites based on Al_2O_3, SiO_2 and IG-017 additive. *IOP Conf. Ser.: Mat. Sci. Eng.,* Vol. 175, p. 012013.
http://dx.doi.org/10.1088/1757-899X/ 175/1/012013

[15] Gömze, L. A., Kulkov, S. N., Kurovics, E., Buyakov, A. S., Buzimov, A. Y., Grigoriev, M. V., Kanev, B. I., Kolmakova, T. V., Levkov, R. V., Sitkevich, S. A. (2018). Development ceramic composites based on Al_2O_3, SiO_2 and IG-017 additive. *Építőanyag – JSBCM,* 70 (1), p. 13.
https://doi.org/10.14382/epitoanyag-jsbcm.2018.3

[16] Grigoriev, M. V., Savchenko, N. L., Sablina, T. Yu., Kurovics, E., Sevostyanova, I. N., Buyakova, S. P., Gömze, L. A., Kulkov, S. N. (2018). Deformation and fracture of alumina ceramics with hierarchical porosity. *Építőanyag – JSBCM,* 70 (1), p. 18.
https://doi.org/10.14382/epitoanyag-jsbcm.2018.4

[17] Reschke, V., Laskowsky, A., Kappa, M., Wang, K., Bordia, R. K. & Scheffler, M. (2011). Polymer derived ceramic foams with additional strut porosity. *Építőanyag – JSBCM,* 63 (3–4), p. 57.
http://dx.doi.org/10.14382/epitoanyag-jsbcm.2011.10

[18] Chu, H. L., Wang, C. L., Lee, H. E., Sie, Y. Y., Chen, R. S., Hwang, W. S. & Wang, M. C. (2013). Effect of sintering process parameters on the properties of 3Y-PSZ ceramics. *IOP Conf. Ser.: Mater. Sci. Eng.,* Vol. 47, p. 012005.
http://dx.doi.org/10.1088/1757-899X/47/1/012005

[19] Ainabayev, A., Arkhipov, M., Baideldinova, A., Omarova, k. & Ksandopulo, G. (2013). Out-of-Furnace Synthesis of High-Temperature Ceramic Materials in the Revolving Reactor. *IOP Conf. Ser.: Mater. Sci. Eng.,* Vol. 47, p. 012044.
http://dx.doi.org/10.1088/1757-899X/47/1/012044

[20] Gömze, L. A. (2016). *Applied materials science I – Compilation of Selected Scientific Papers I.* Published by IGREX Ltd (Hungary), pp. 1–189.

[21] Sadowski, T. & Golewski, P. (2016). The use of experimental bending tests to more accurate numerical description of TBC damage process. *IOP Conf. Ser.: Mater. Sci. Eng.,* Vol. 123, p. 012017. http://dx.doi.org/10.1088/1757-899X/123/1/012017

[22] Kurovics, E., Buzimov, A. Y., Gömze, L. A. (2016). Influence of raw materials composition on firing shrinkage, porosity, heat conductivity and microstructure of ceramic tiles. *IOP Conf. Ser.: Mater. Sci. Eng.,* Vol. 123, p. 012058.
http://dx.doi.org/10.1088/1757-899X/123/1/012058

[23] Zharikov, E. V., Kapustyn, V. V., Faikov, P. P., Popova, N. A., Barmin, A. A., Ivanov, A. V. & Rizakhanov, R. N. (2017). Preparation of SiC–MgAl$_2$O$_4$–Y$_3$Al$_5$O$_{12}$-MWCNTs nanocomposites by spark plasma sintering. *IOP Conf. Ser.: Mater. Sci. Eng.,* Vol. 175, p. 012065. http://dx.doi.org/10.1088/1757-899X/175/1/012065

[24] Kurovics, E., Gömze, L. A. (2017). Influence of sintering atmosphere and IG-017 bio-original additives on porosity of ceramics made from high purity Al$_2$O$_3$ and SiO$_2$ in *MultiScience – XXXI. microCAD International Multidisciplinary Scientific Conference University of Miskolc,* Hungary, 20–21 April, 2017.

[25] Kurovics, E., Gömze, L. A. (2017). Development of high-tech ceramic composites from conventional kaolinite minerals and IG-017 additives. in *MultiScience – XXXI. microCAD International Multidisciplinary Scientific Conference University of Miskolc,* Hungary, 20–21 April, 2017.

[26] Buyakov, A. S., Levkov, R. V., Buyakova, S. P., Kurovics, E., Gömze, L. A., Kulkov, S. N. (2018). Formation of Pore Structure in Zirconia-Alumina Ceramics. *Építőanyag – JSBCM,* 70 (1), p. 27.
https://doi.org/10.14382/epitoanyag-jsbcm.2018.6

[27] Miranda-Hernández, J. G., Rocha-Rangel, E., Díaz de la TorreS. (2010). Synthesis, microstructural analysis and mechanical properties of alumina-matrix cermets. *Építőanyag – JSBCM,* 62 (1), p. 2.
http://dx.doi.org/10.14382/epitoanyag-jsbcm.2010.1

[28] Rocha-Rangel, E., Hernández-Silva, D., Terrés-Rojas, E., Martínez Franco, E., Díaz-de la Torre, S. (2010). Alumina-based composites strengthened with titanium and titanium carbide dispersions. *Építőanyag – JSBCM,* 62 (3), p. 75.
http://dx.doi.org//10.14382/epitoanyag-jsbcm.2010.15

[29] Gömze, L. A. & Gömze, L. N. (2010). Mechanical stress relaxation in hetero-modulus, hetero-viscous complex ceramic materials. *Építőanyag – JSBCM,* 62 (4), p. 98. http://dx.doi.org//10.14382/epitoanyag-jsbcm.2010.18

[30] Savchenko, N. L., Sablina, T. Yu., Sevostyanova, I. N., Buyakova, S. P., Kulkov, S. N. (2015). Deformation and Fracture of Porous Brittle Materials Under Different Loading Schemes. *Russ. Phys. J.,* Vol. 58, p. 1544, 2016, translated from Izvestiya Vysshikh Uchebnykh Zavedenii, Fizika, No. 11, pp. 56–60, November, 2015. Available: https://doi.org/10.1007/s11182-016-0680-4.

[31] Gömze, L. A., Gömze, L. N. (2017). Rheological principles of development hetero-modulus and hetero-viscous complex materials with extreme dynamic strength. *IOP Conf. Ser.: Mat. Sci. Eng.,* Vol. 175, p. 012001
https://doi.org/10.1088/1757-899X/175/1/012001

[32] Kolmakova, T. V., Buyakova, S. P. & Kulkov, S. N. (2018). Modeling of Bone Tissue Structure and Porous Ceramics. *J. Phys.: Conf. Ser.,* Vol. 1045, p. 012022. https://doi.org/10.1088/1742-6596/1045/1/012022

[33] Gömze, L. A. & Gömze, L. N. (2013). Ceramic based lightweight composites with extreme dynamic strength. *IOP Conf. Ser.: Mater. Sci. Eng.*, Vol. 47, p. 012033. https://doi.org/10.1088/1757-899X/47/1/012033

[34] Gömze, L. A., Liszátzné Helvei, Á., Simonné Odler, A., Szabó, M. (2001). *Ceramic yearbook I. 2001.* Budapest: ÉTK and MÉASZ, pp. 30–85.

[35] Duval, D. J., Risbud, S. H., Shackelford, J. F. (2008). Mullite. In *Ceramic and Glass Materials*. Shackelford, J., Doremus, R. H. ed., Springer. http://www.springer.com/978-0-387-73361-6

[36] Bobkova, N. M (2007). *Fizicheskaya Himiya Tugoplavkih Nemetallicheskih i Silicatnyh Materialov*. Minszk: Yvyshej Shaya, pp. 88–90.

[37] Varga, G. (2007). The structure of kaolinite and metakaolinite. *Építőanyag – JSBCM,* 59 (1), p. 6. http://dx.doi.org/10.14382/epitoanyag-jsbcm.2007.2

[38] Schneider, H., Schreuer, J., Hildmann, B. (2008). Structure and properties of mullite — A review. *Journal of the European Ceramic Society,* 28, pp. 329–344. http://dx.doi.org/10.1016/j.jeurceramsoc.2007.03.017

[39] Gömze, L. A., Gömze, L. N. (2010). Hetero-Modulus Nanoparticles Reinforced Corundum Matrix CMC with Extreme Wear and Thermal Shock Resistances. *Materials Science Forum,* Vol. 659, p. 165. https://doi.org/10.4028/www.scientific.net/MSF.659.165

[40] Gömze, L. A., Gömze, L. N. (2012). Advanced Hetero-Modulus and Hetero-Viscous Complex Materials. *Materials Science Forum,* Vol. 729, p. 43. https://doi.org/10.4028/www.scientific.net/MSF.729.43

[41] Gömze, L. A., Gömze, L. N., Egész, Á. & Ojima, F. (2013). High Porosity Alumina as Matrix Material for Composites of Al-Mg Alloys. *IOP Conf. Ser.: Mater. Sci. Eng.*, Vol. 47, p. 012030. https://doi.org/10.1088/1757-899X/47/1/012030

[42] Gömze, L. A. (2015). *RHEOLOGY Compilation of Scientific Papers I*. Published by IGREX Ltd (Hungary), pp. 1–195.

[43] Heimann, Robert B. (2010). *Classic and Advanced Ceramics*. Weinheim: Wiley-VCH Verlag GmbH & Co. KGaA.

[44] Vakalova, T. V., Govorova, L. P., Reshetova, A. A., Tokareva, A. Y., Shvagrukova, E. V. (2014). Activation of Synthesis and Sintering of Mullite Aluminosilicate Ceramics Based on Natural Raw Materials. *Advanced Materials Research,* 1040, pp. 268–271. http://dx.doi.org/10.4028/www.scientific.net/AMR.1040.268

[45]   Sternitzke, Martin (1997). Structural ceramic nanocomposites. *Journal of the European Ceramic Society,* Vol. 17, pp. 1061–1082. https://doi.org/10.1016/S0955-2219(96)00222-1

[46]   Carter, C. Barry, Norton, M. Grant (2013). *Ceramic Materials Science and Engineering*. Springer, pp. 336–350.

[47]   Gustafsson, S., Falk, L. K. L., Pitchford, J. E., Clegg, W. J., Lidén, E., Carlström, E. (2009). Development of microstructure during creep of polycrystalline mullite and a nanocomposite mullite/5 vol.% SiC. *Journal of the European Ceramic Society,* Vol. 29, pp. 539–550. https://doi.org/10.1016/j.jeurceramsoc.2008.06.036

[48]   Yoshio Sakka (1995). Processing of Silicon Carbide-Mullite-Alumina Nanocomposites. *Journal of the American Ceramic Society,* 78 (2), pp. 479–486. https://doi.org/10.1111/j.1151-2916.1995.tb08827.x

[49]   Lin, Chien-Cheng, Zangvil, Avigdor, Ruh, Robert (2000). Phase Evolution in Silicon Carbide–Whisker-Reinforced Mullite/Zirconia Composite during Long-Term Oxidation at 1000° to 1350 °C. *Journal of the American Ceramic Society,* 83 (7), pp. 1797–1803. https://doi.org/10.1111/j.1151-2916.2000.tb01466.x

[50]   Akpinar, S., Kusoglu, I. M., Ertugrul, O., Onel, K. (2012). Silicon carbide particle reinforced mullite composite foams. *Ceramics International,* Vol. 38, pp. 6163–6169. https://doi.org/10.1016/j.ceramint.2012.04.067

THE EFFECT OF STRUCTURAL CHANGES
ON THE MECHANICAL PROPERTIES
OF PVC/WOOD COMPOSITES

KRISZTINA ROMÁN[1]–KÁLMÁN MAROSSY[2]

The relationship between structure and mechanical properties of neat PVC and PVC/Wood composite were investigated in this study. The mechanical properties, visual appearances and morphology of the composites were examined by varying the wood filler content in the composites. The hardness, the tensile-, and flexural- properties of the composite were considerably decreased. In the results of the mechanical test the ultimate strengths were increased with decreasing elongation at break. The decreases can be explained the presence of moisture in the wood. The experimental results showed that the wood fibre additive has modifier effects on the mechanical properties of PVC. Increasing density values achieved by using wood fibre. Furthermore, the effect of viscoelastic properties of PVC/Wood-flour materials can be examined. The filler behaves as modifier that significantly increases the melt viscosity of the PVC.

Keywords: composite, melt viscosity, mechanical properties

INTRODUCTION

In the last 20 years, natural organic fillers have been regularly applied in the global market. Poly(vinyl-chloride)/Wood composite are recently popular in many applications, particular in the construction industries [1]. The reason is the desirable properties of the composite such as the relative low cost and the abrasion resistance [2]. Furthermore, the composites are environmentally friendly and recyclable [1]. Studies have pointed out the main problems, the strength of the composites decrease, the leaching of the additives and the deterioration of the physical properties of the blend [3]. The wood additives are sensitive to thermal degradation; therefore it was only suitable for some type of plastics, such as PVC, PE and PP. However, it is very difficult to reach strong adhesion between hydrophilic cellulose and hydrophobic polymer (PVC). Studies have used three general opportunities to enhance dispersion and compatibility of cellulose with polymers: fiber-, matrix- and interface treatment [4].

The advantages of wood are: low apparent density, excellent mechanical properties and good biodegradation [1]. Unfortunately, it has negative aspects as well: sensitivity

---

[1]   Institute of Ceramics and Polymer Engineering, University of Miskolc
       H-3515 Miskolc-Egyetemváros, Hungary
       polkrisz@uni-miskolc.hu
[2]   Institute of Ceramics and Polymer Engineering, University of Miskolc
       H-3515 Miskolc-Egyetemváros, Hungary
       polkal01@uni-miskolc.hu

to UV radiation, biological attack, degradation from high temperatures and the air moisture. Therefore the service lives of the composites need to be extended [5].

In the past decades, several investigations were carried out for foaming of PVC/Wood composites and their extrusion processes [6]. Some studies worked on investigation of rheological properties of the PVC/Wood composite. The high melt viscosity of PVC blends can be measured by extrusion. It was concluded that the properties of composites lead to poor quality [7]. The results of the rheological and mechanical tests presented in this paper can help us to make comprehensive conclusion about the composites structures and usability's. The tests can also be used to identify the possible processing problems. The aim of the present study is to examine the PVC/Wood-flour composites in order to evaluate and compare its suitability for building and construction industry.

1. MATERIALS

The ingredients of PVC composites are commercial products; suspension grade PVC (K value = 58), solid Ca-Zn based stabilizer, external- and internal lubricants, ground $CaCO_3$ filler, acrylic based processing aid and wood-flour. Azodicarbonamide (1.5 phr) was used as foaming agent. The amount of the wood flour component was 20 phr.

1.1. Sample preparation

PVC compounds were mixes with dry-blend by using a high-speed mixer. From the mixtures extruded sheets were preparedin a twin screw extruder. The final sheets were about 4 mm thick. The blending temperatures in the extruder were 165 to 180 °C.

The extruded sheets were directly used to prepare the samples. Most of the measurements were carried out on the samples both in machine- and cross direction. The reason for that was the determination of the anisotropic nature of specimens, since the processing parameters will be affecting the final foamed structures.

1.2. Examination of rheological properties

The aim of these tests is assessing the flow behaviour and to explain some technological problems. The composite's morphology mostly depends on the concentration of pure components, the material matrix and the wood flour additive [8]. The rheological tests were carried out on a Göttfert Extrudiometer 20 laboratory measuring extruder. The barrels diameter 20 mm, the length is 20D (400 mm). A continuous compression screw of 1 : 4 compression rate was used. The die (capillary) was flat die; 1 mm thickness, 10 mm width and 30 mm length. Barrel temperature at were set 180 to 200 °C. All data (3 pressure date, 3 steel temperatures, 3 mass temperatures; output, torque) were recorded at 20, 40, 60, 80, 100 rpm. P3 (pressure in front of capillary inlet) and G (output, g/min) data were used for calculations.

The viscosity values of the materials can be determined using different correlations. The viscosity (η) is the quotient of shear stress and shear rate. These data can be easily obtained on the wall capillary.

$$\tau = \frac{h \, \Delta P}{\left(\frac{h}{w} + 1\right) 2 \, l} \tag{1}$$

Where:
τ – shear stress [MPa],
h – thickness of the gap [mm],
w – width of the gap [mm],
ΔP – pressure drop on the capillary [Pa],
l – length of the gap [mm].

Bagley (length) correction was not calculated because we had no flat dies of different lengths.

$$\dot{\gamma} = \frac{6 \, Q}{h^2 w} \left(\frac{n+2}{3}\right) \tag{2}$$

Where:
$\dot{\gamma}$ – calculated shear rate [1/s],
Q – volumetric speed [m^3/s],
h – thickness of the gap [mm],
w – width of the gap [mm],

$$n = \frac{d \lg Q}{d \lg \Delta P} \tag{3}$$

Where:
n – flow exponent (Rabinovits correction),
Q – volumetric speed [m^3/s],
ΔP – pressure drop on the capillary [Pa].

The Rabinovits exponent "n" was calculated from the reciprocal slope of lg (P3) – lg (G) straight line.
The viscosity [Pas] is:

$$\eta = \frac{\tau}{\dot{\gamma}} \tag{4}$$

From the equations of stress (1) calculates sheer rate (2) and flow exponent (3) the viscosity (4) of the material can be determined.

1.3. Mechanical properties

The tensile tests were performed on INSTRON 5566 universal testing machine according to ASTM D389 standard at room temperature (23 ± 1 °C). The cross-head speed was 100 mm/min. The flexural test was evaluates using three point bending

head supplied by INSTRON 5566 model. The method was followed the ISO 178:2010 international standard. Seven specimens were testes from each sample both for tensile and flexural tests.

The hardness test was carried out with Zwich/Roell machine using duromer Shore D punching tool. The method procedure was specified by ISO 868 standard. Twenty locations were measured from each sample.
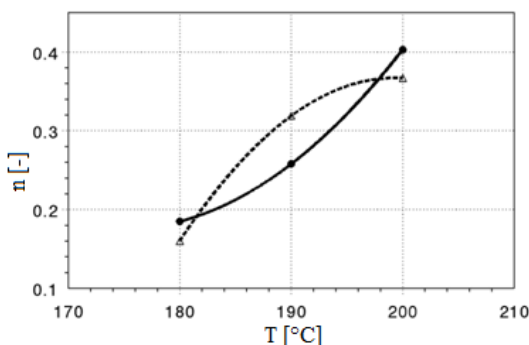
2. RESULTS AND DISCUSSION
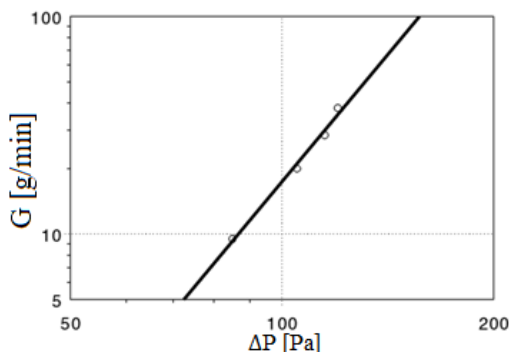
Figure 1

Example of determination of n exponent (sample: PVC/Wood at 190 °C)

The calculated flow exponents show that the higher is the melt temperature the higher is the "n". That means that the flow tends to Newtonian by increasing temperature. It is valid both for the neat PVC and the PVC/Wood composite.
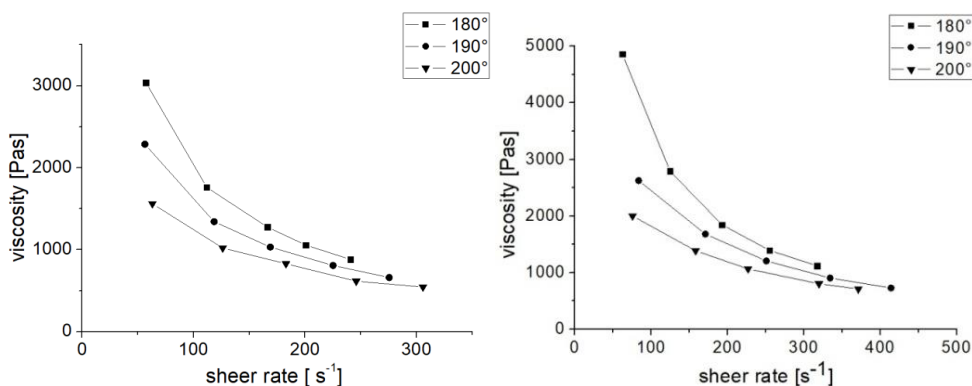

Figure 2

Calculated flow exponents; solid line: PVC/Wood, dashed line: neat PVC

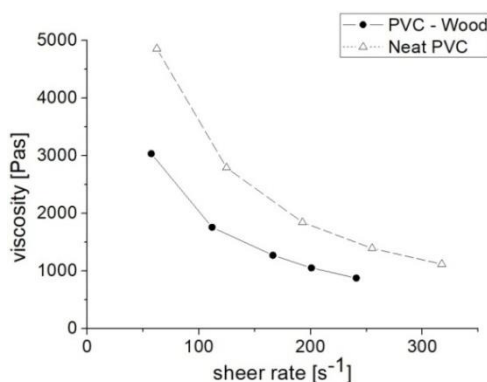The measurements were carried out with different temperature settings.
160, 170, 180 °C,
170, 180, 190 °C and
180, 190, 200 °C (from feeding to die).

Figure 3
Flow curves (viscosity vs. shear rate) of PVC/Wood (left) and neat PVC (right)

Figure 4
Flow curves of neat PVC (dashed line) and PVC/Wood composite (solid line)

The content of wood (20 phr) modified the viscosity of the PVC/Wood composite. Nevertheless it necessary to take into accounts this modification in the processing. It probably cause processing failures and the final product will be defective. It does not appropriate the most technical requirements.

2.1. Density and hardness tests

Density values were determined by water immersion measurement with a Mettler-Toledo digital analytical scale fitted with Archimedes accessory.

The hardness tests were carried out using a Zwick/Roell Ho.43150 type digital Shore D test equipment. The Shore D test method is used for harder plastics and elastomers, so it is well suitable for measuring the PVC composite samples. The tests were carried out according to ISO 868 standard. On each specimens of four mm thickness 20 parallel measurements were made to determine the mean values and standard deviation.

2.2. Tensile tests

Stress-strain curves of neat PVC and PVC/Wood composite were compared. The tensile tests curves show that the elongation at break strongly decreased by the wood-flour. However, the tensile strength of the blend increased compared to the neat PVC foam. *Table 1* contains the result of the test.

Table 1

Maximum values of tensile strength in machine- and cross direction

Materials	Tensile strength [MPa]
Neat PVC – M	18.8 ± 2.3
Neat PVC – C	7.8 ± 0.4
PVC/Wood –M	32.7 ± 0.9
PVC/Wood – C	28.8 ± 0.8

2.3. Flexural tests

The morphology of the composite has significant effect on the flexural behaviour of the material. The modifying effects of wood to PVC foam can be seen from flexural strength and flexural modulus of the blends *(Table 2)*.

Table 2

Results of flexural tests

Materials	Flexural strength [MPa]
Neat PVC – M	22.1 ± 2.8
Neat PVC – C	7.3 ± 0.8
PVC/Wood – M	51.5 ± 2.4
PVC/Wood – C	43.3 ± 1.4

It is observed that the blends in general display significantly lower deformations at the breakpoints than the neat PVC foam. The flexural stain values of PVC foam at breakpoint increased, but yield strength and elastic modulus decreased. Generally, the properties in machine direction has higher strength values, than in the cross direction. Based on *Table 2* the flexural strength of the PVC foam – M is approximately the half of the PVC/Wood – C's. The flexural results show similar behaviour to the tensile test results.

2.4. Hardness tests

Significant increase was observed in case of wood flour containing samples. The Shore D hardness of neat PVC is 39.7; PVC/Wood composite has a Shore D 64.7.

SUMMARY

Our aim was to examine the rheological and the mechanical properties of PVC/Wood composite and PVC. Two different types of composite had been prepared in granulate and extruded sheet form and tested. The results of the tests give information about the viscosity values and the mechanical properties of the materials such as hardness, tensile-, and flexural properties. The neat PVC melt flow resulted higher viscosity values compares to the PVC-Wood composite. It is important to emphasize that these viscosity parameters are in dispensable for assessment of processing behaviour.

     The wood flour has significant reinforcing effect proved by tensile-, flexural and hardness tests. The formulation did not contain any "compatibilizing" additive; interestingly the composite worked perfectly probably because of the polar nature of PVC.

     The melt viscosity curves are regular following the power law. The increase of viscosity is about 30–40%, slightly higher than expected from the assessed volume fraction of wood. Due to the foamed structure, the determination of the accurate volume fraction was not possible.

ACKNOWLEDGMENT

REMARK

The content of this paper has been partly presented at the MultiScience XXXIInd MicroCad International Scientific Conference, 5–6 September, 2018, Miskolc, Hungary.

REFERENCES

[1]   Jiang, H. & Kamdem, D. P. (2004). Development of poly(vinyl chloride)/ wood composites. A literature review. *Journal of Vinyl and Additive Technology*, Vol. 10, No. 2, pp. 59–69.

[2]   Kositchaiyong, A., Rosarpitak, V., Hamada, H. & Sombatsompop, N. (2014). Anti-fungal performance and mechanical-morphological properties of PVC and wood/PVC composites under UV-weathering aging and soil-burial exposure. *International Biodeterioration and Biodegradation*, Vol. 91, pp. 128–137.

[3]   Pilarski, J. M. & Matuana, L. M. (2006). Durability of wood flour-plastic composites exposed to accelerated freeze-thaw cycling. II. High density polyethylene matrix. *Journal of Applied Polymer Science*, Vol. 100, No. 1, pp. 35–39.

[4]   Doroudiani, S. (1999). Microcellular wood-fibre thermoplastic composites: processing-structure-properties. Ph.D. dissertation, Department of Chemical Engineering and Applied Chemistry, University of Toronto.

[5]   Roberts, W. T. & Davidson, P. M. (1986). Growth characteristics of selected fungi on polyvinyl chloride film. *Applied and Environmental Microbiology*, Vol. 51, No. 4, pp. 673–676.

[6]   Matuana, L. M. & Mengeloglu, F. (2002). Manufacture of rigid PVC/wood-flour composite foams using moisture contained in wood as foaming agent. *Journal of Vinyl and Additive Technology*, Vol. 8, No. 4, pp. 264–270.

[7]   Shah, B. L. & Matuana, L. M. (2004). Online measurement of rheological properties of PVC/wood-flour composites. *Journal of Vinyl and Additive Technology*, Vol. 10, No. 3, pp. 121–128.

[8]   Bhaskar, J., Haq, S., Pandey, A. K. & Srivastava, N. (2012). Evaluation of properties of propylene-pine wood plastic composite. *Journal of Materials and Environmental Science*, Vol. 3, No. 3, pp. 605–612.